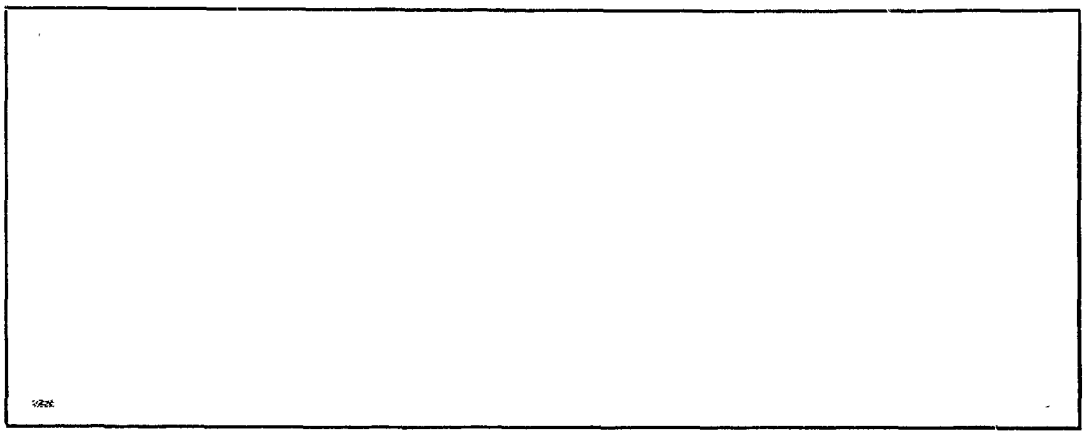

ADVANCED KINETICS

COSTA MESA CALIFORNIA

GPO PRICE $ _____

CFSTI PRICE(S) $ _____

Hard copy (HC) $4.00

Microfiche (MF) .75

ff 653 July 65

3/6/13

A D V A N C E D K I N E T I C S, I N C.

"NEW CONCEPTS FOR HIGH ENERGY RATE FORMING SYSTEM"

Contract NAS 8-11758

SUMMARY REPORT

Prepared for

NATIONAL AERONAUTICS AND SPACE ADMINISTRATION
GEORGE C. MARSHALL SPACE FLIGHT CENTER
HUNTSVILLE, ALABAMA

August 27, 1965

ADVANCED KINETICS, INC.

This report was prepared by the ADVANCED KINETICS, INC. under Contract NAS 8-11758 for the George C. Marshall Space Flight Center, National Aeronautics and Space Administration. The work was administered by the George C. Marshall Space Flight Center.

A D V A N C E D K I N E T I C S, I N C.

This report was prepared by ADVANCED KINETICS, INC. under Contract NAS 8-11758 for the George C. Marshall Space Flight Center, National Aeronautics and Space Administration. The work was administered under the technical direction of the Propulsion and Vehicle Engineering Laboratory, Materials Officer's Technical Representative, acting as project manager.

The following personnel has contributed to the performance of this project:

Dr. R. W. Waniek

Dr. H. P. Furth

Mr. W. L. Lobdell

Mr. P. J. Jarmuz

Mr. J. C. Hartley

Mr. D. R. Holt

Mr. D. M. Fitzgerald

Mr. T. Emil

Mr. R. C. Mehra

Mr. H. J. Gilsdorf

Mr. G. N. Cirica

TABLE OF CONTENTS

LIST OF ILLUSTRATIONS

LIST OF ILLUSTRATIONS (Continued)

LIST OF ILLUSTRATIONS (Continued)

1) INTRODUCTION

High pressure waves created by a plane magnetically actuated diaphragm have been studied theoretically and experimentally. In regard to the generation and propagation of an acoustic wave, if we denote the sonic velocity in the fluid as c and the fluid displacement is

$$d = d_o e^{ik(ct + z)} \tag{1}$$

then the fluid velocity has amplitude

$$v_o = kd_o c \tag{2}$$

$$= 2\pi \frac{d_o}{\lambda} c \tag{2a}$$

where $\lambda = 2\pi/k$ is a full wavelength of the pressure pulse. The fluid acceleration has amplitude

$$a_o = k^2 d_o c^2 \tag{3}$$

and so the diaphragm pressure required to actuate the wave amplitude is given as

$$p_o = \rho k d_o c^2 \tag{4}$$

where ρ is the mass density of the fluid. The energy input per unit area in a half cycle is

$$E = \int_o^{\pi/kc} pv\,dt = \rho k d_o^2 c^2 \tag{5}$$

In consonance with theoretical considerations a qualitative and quantitative investigation of the pressure pulse phenomenon in the liquid medium has

been carried out. This study has been facilitated by the employment of transducer technology in the pressure measurements.

The design and engineering of an optimized magnetohydraulic forming system based upon the earlier determined theoretical principles has been conducted.

Experimental studies utilizing various modes of operation have been made with regard to both pressure and deformation measurements. Optimization of the pressure pulse has been carried out by the observation of the effective forming ability of the system in the various operational modes.

An inductive storage device and interrupter element has been designed and constructed. The system has been optimized in regard to the switching efficiency.

II) ACOUSTIC TECHNOLOGY WITH PRESSURE TRANSDUCER

Of initial interest in the experimental phase of the program was the development of methods which would permit qualitative and quantitative observations of the acoustic pressure pulse. For this purpose an optimized acoustical pickup line and a transducer element were developed. Prior to the construction and utilization of the transducer assembly, it was necessary to investigate the technology of piezoelectric crystals and ceramics as detectors of acoustic power.

A) TRANSDUCER TECHNOLOGY

A piezoelectric crystal exhibits the property of becoming electrified upon the application of pressure, or, conversely, of deforming in an electric field. The essential feature which permits this type of operation is the structural bias of the crystal and the resulting polarization due to the applied stress. The employment of a piezoelectric transducer is generally in the form of a traveling wave arrangement for the measurement of sonic pulses of short duration. In this type of device, a piezoelectric crystal is sandwiched between two sections of the acoustical line. Optimum contact is made to insure minimum reflection at the boundaries. The pressure pulse travels along the initial section of the line and is incident upon the face of the crystal where a charge is generated. The reflections which are due to the

discontinuities at the boundaries may be reduced by matching the acoustic impedance of the elements involved.

The acoustic impedance of a medium is defined as the ratio of acoustic pressure to associated particle velocity, or

$$Z = p/u \tag{6}$$

where p = acoustic pressure and u = particle velocity.

For a plane progressive wave, this ratio is given by the formula

$$Z = \rho_o c \tag{7}$$

where ρ_o = density of medium and c = longitudinal velocity of wave. The MKS unit of acoustic impedance is kg/m^2sec.

The condition for passage of the wave without reflections requires that the reflection coefficient be zero, hence

$$R = (Z_2 - Z_1)/(Z_2 + Z_1) = 0 \tag{8}$$

and therefore $Z_2 = Z_1$.

The transmission coefficient is given by the equation

$$T = 2Z_2 / (Z_2 + Z_1) \tag{9}$$

and this is a maximum when $Z_2 = Z_1$.

In many cases, the transmitted wave is an attenuated one because it is very difficult to match exactly the impedance of the media. The characteristic impedances of various materials are given in Table I on the following page.

TABLE I

ACOUSTIC IMPEDANCES OF VARIOUS MATERIALS

Material	Density 10^3 kg/m^3	Young's Modulus 10^{10} new/m^2	Longitudinal Wave Velocity m/sec	Characteristic Impedance kg/m^{2}sec
Aluminum	2.7	7.1	5140	13.9×10^6
Brass, yellow	8.6	10.4	3490	30.0×10^6
Copper	8.9	12.2	3560	31.7×10^6
Duralumin 175	2.8	17.2	7850	22.0×10^6
Gold, hard	19.3	8.1	2050	39.6×10^6
Iron, pure	7.86	20.6	5120	40.3×10^6
Lead	11.34	1.5	1160	13.2×10^6
Magnesium	1.74	4.2	4910	8.6×10^6
Nickel	8.9	21.4	4900	43.6×10^6
Silver	10.5	7.5	2680	28.2×10^6
Tin	7.3	5.5	2740	20.0×10^6
Zinc	7.2	10.5	3820	27.5×10^6
Barium Titanate	5.4	11.1	4540	24.5×10^6
Quartz	2.6	7.9	5500	14.3×10^6
Fused Silica	2.2	7.3	5760	12.7×10^6
Pyrex	2.3	6.2	5200	12.0×10^6
Nylon 6-6	1.11	0.36	1800	2.0×10^6
Lucite	1.18	0.40	1840	2.2×10^6
Water	1.0		1481	1.48×10^6
Mercury	13.6		1450	19.7×10^6
Alcohol, ethyl	0.79		1150	0.91×10^6
	kg/m^3			
Air	1.33		331	429
Argon	1.78		319	569
Helium	0.178		970	173
Hydrogen	0.088		1270	114
Oxygen	1.43		317	453

Values of the transmission coefficient for various interfaces are presented in Table II.

TABLE II

CALCULATIONS OF TRANSMISSION COEFFICIENT AT VARIOUS INTERFACES

Interface	Transmission (%)
Water - Aluminum	35.2
Water - Brass	18.3
Water - Lead	36.6
Water - Silver	19.3
Water - Zinc	19.7
Water - Fused Silica	37.6
Water - Quartz	34.6
Water - Nylon	97.5
Water - Lucite	96.4
Nylon - Barium Titanate	28.0
Lucite - Barium Titanate	30.4
Lead - Barium Titanate	91.4
Zinc - Barium Titanate	99.5
Silver - Barium Titanate	99.0
Aluminum - Barium Titanate	91.5

For a number of interfaces the transmission coefficient is given by

$$\alpha = \prod_{1}^{n} \alpha_n$$

Interface	Transmission (%)
Water - Aluminum - Barium Titanate	32.2
Water - Nylon - Barium Titanate	27.3
Water - Lucite - Barium Titanate	29.3
Water - Lead - Barium Titanate	33.4
Water - Silver - Barium Titanate	19.1

As the pulse traverses the crystal, it generates a voltage which is proportional to the pressure. This voltage is given by the equation

$$V = (d_{33}\, x/k\epsilon_o)\, p \qquad (10)$$

where d_{33} is piezoelectric constant, x the thickness of the crystal, $k\epsilon_o$ the dielectric constant, and p is the acoustic pressure.

B) DESIGN AND DEVELOPMENT OF TRANSDUCERS

Two transducer assemblies have been designed and constructed for the observation and measurement of the acoustic pressure waves generated in the fluid medium. In both cases, the piezoelectric crystal utilized has been the ceramic perovskite, barium titanate, Ba Ti O_3 , a crystal of tetragonal form in the temperature range 5°C - 120°C.[1] Operated in the thickness mode the crystal exhibits the following properties:

Density	5.5×10^3 kg/m^3
Curie Point	120°C
Coupling Coefficient (k_{33})	0.46

The essential differentiation in the construction of the two transducer assemblies was in regard to their utilization. The initial acoustic line was designed for operation with only the receiving part of the line immersed in the liquid medium. A schematic illustration of this instrument is presented in Fig. 1.

The device features a barium-titanate crystal which is bonded by soft silver soldering to two aluminum rods. The rod which first receives the incident pressure pulse is a tapered aluminum rod with length equal to 12.5". The cross-sectional area of this rod at any point is given by the equation

$$A = A_o (mx + 1)^2 \qquad (11)$$

where m is a constant related to the flare of the tapered rod. The second rod is cylindrical with length equal to 8". As noted in Fig. 1, there is a hole tapped into the end of the rod. In this cavity, aluminum microspheres were placed to reduce the reflection of waves back toward the crystal. The main advantage in utilizing a tapered rod design is that the dimensions of the free end of the rod can be minimized to allow good spatial resolution in the scanning of the sonic field. The flare constant is kept small so that the waves retain the form of a plane progressive wave.

Pressure transducers are operated below resonant frequencies to insure the absence of mechanical vibrations in the crystal which would result in spurious readings. The resonant frequency of a crystal is a function of the frequency constant and the controlling dimension. The barium-titanate crystal used in this device has a resonant frequency of 11 Mc and, consequently, an upper limit for the operation of the device is established.

The second transducer system was designed for utilization in the liquid medium. This feature necessitated a watertight sealing of the system and the ancillary electrical contacts. Figure 2 is an illustration of the device showing the location of the crystal and sealing mechanisms.

The resonant frequency of this transducer system is 1.1 Mc. The operation is in the thickness mode, similar to the initially developed system.

C) CALIBRATION PROCEDURES

Calibration at low frequencies has been carried out using a pendulum method. A sphere of mass, m, is suspended by a nylon thread of length, L, and held a distance, w, from the tip of the transducer. When the sphere is released and collides with the tip of the tapered rod, it imparts a pulse which travels down the rod to the crystal. From the equation for an impulse we have

$$I = \int_{t_1}^{t_2} F\,dt \tag{12}$$

Employing a Newtonian relationship we obtain

$$I = m\int_{v_2}^{v_1} dv = mv_1 + mv_2 \tag{13}$$

When the pressure pulse reaches the crystal it generates a voltage, V, which is proportional to the pressure, $P = F/A$, such that

$$V = k(F/A) \tag{14}$$

We may thus set up an equation which would permit the evaluation of the system constant by the pendulum calibration method. We obtain

$$K = \int F\,dt / \int V\,dt = m(v_1 + v_2) / \int V\,dt \qquad (15)$$

It is necessary at this point to experimentally determine the coefficient of restitution of the pendulum mass as it rebounds from the transducer tip. It was observed that the mass rebounds approximately two-thirds of its initial distance w. Thus, we have $w_2 = 2w_1/3$. Utilizing the relationship, $v = (2gh)^{1/2}$, it is now possible to obtain the value of the system constant K in equation (15). The numerator is evaluated by the observation of the physical parameters of the system and the denominator is the integrated signal from the pickup crystal displayed on an oscilloscope.

The following sample calibration of the initially developed transducer system illustrates the method described above. The diagram below details the arrangement of the physical parameters of the pendulum.

L = 238 cm

w = 25 cm

m = 17.7 grams

g = 980 cm/sec^2

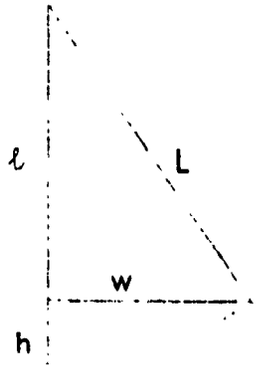

The integrated voltage response of the piezoelectric crystal for the pendulum calibration with the above physical parameters was 1.28×10^{-4} volt-sec. For the evaluation of the physical constant K we have

$$K = \int F dt / \int V dt = \frac{14.971 \times 10^2 \text{ gm-cm/sec}}{1.28 \times 10^{-4} \text{ volt-sec}} =$$

$$= 11.64 \times 10^6 \text{ dynes/volt}$$

The area of the tip of the tapered rod is equal to 2.22×10^{-2} cm^2. Consequently, we obtain for the pressure constant, K

$$K = \left(\frac{11.64 \times 10^6 \text{ dynes/volt}}{2.22 \times 10^{-2} \text{ cm}^2}\right) \cdot \left(9.87 \frac{\text{atm}}{\text{dyne/cm}^2}\right) = 518.3 \text{ atm/volt.}$$

III) COIL DESIGN AND DEVELOPMENT

Within the scope of work under Contract NAS 8-11758, this facility has carried out the design and development of two devices for the generation and propagation of pressure waves in the liquid medium in consonance with the theoretical considerations. In addition, utilization was made of the experimental studies which were conducted as a complementation of the formulation of the hydromagnetic theory.

A) 20 KILOJOULE DEVICE

The engineering and design of a magnetically driven hydraulic hammer for an input of 20 kilojoules was carried out in accordance with the previously developed theoretical and experimental criteria for the optimization of hydromagnetic pulse generation.

The device consists of a 6" diameter coil having a total of 18 turns. The current feedthrough is a high amperage, low inductance rigid coaxial system five feet in length. The current feedthrough is attached to two square parallel plates, one of which serves as a ground. The plates are further bolted at the edge for structural stability and to prevent deformation due to mechanical shock. Energy to the parallel plates is supplied by 14 flexible coaxial cables from the capacitor bank. Handles

are also provided to facilitate movement of the device. The device is insulated for operation up to 20 kv.

The coaxial feeder line possesses the following features required for this application:

1) Strength to counteract mechanical stresses on the conductors due to the high transient currents;
2) Maintaining a watertight seal in spite of the mechanical shock created by the recoil action of the device;
3) A low inductance to achieve efficient energy transfer into the load.

The coaxial geometry exhibits an inductance per unit length of

$$L = 2 \times 10^{-7} \left[\ell n \, (a_2 / a_1) + (1/4\pi) (10^7 / f\sigma)^{1/2} (a_1 + a_2 / a_1 \, a_2) \right] \quad (16)$$

where a_1 and a_2 are the radii of the inner and outer conductors, f is the frequency, and σ is the conductivity of the material.

A copper cylinder, 4.8 cm in diameter, separated from its return path by a 0.3 cm insulator, yields an inductance of 16.9 nh/m at a frequency of 10 kc.

The force between the two cylinders during current passage is due to the pressure P_m generated by the magnetic field B. This force is calculated from the formula

$$\Phi \approx LI = B(a_2 - a_1 + 2\delta)\ell \quad (17)$$

and therefore for P_m we have

$$P_m = B^2/2\mu_o = 1/2\mu_o \left[(L/\ell) \cdot (I/a_2 - a_1 + 2\delta) \right]^2 \qquad (18)$$

where L/ℓ is the inductance per unit length, I the current, and δ is the skin depth. For a design value of 10^5 amps, the peak magnetic field will amount to 7 kilogauss and the magnetic pressure will rise to only 25 psi. The outer conductor is fabricated from stainless steel of .120" wall thickness with an ultimate tensile strength of 80,000 - 100,000 psi. With such a large tensile strength and a low magnetic pressure there was justification in precluding the possibility of expansive forming of the tubing.

The geometric and electromagnetic parameters for the 20 kilojoule system are presented in Table III on the following page. In addition, extrapolated parameters for an increased capacitance level are given.

The magnetic field profile for the 20 kilojoule MFH-1 coil delivered to the GCMSFC is presented in Fig. 3. The pressure profile generated by the magnetic field is shown in Fig. 4. Both curves are plotted as a function of radial distance from the center of the coil.

TABLE III

BASIC PARAMETERS OF 20 KILOJOULE 6" MFH COIL

Nominal Radius (cm)	7.62
Conductor Radius (cm)	6.35
Number of Turns	19
Weight (kg)(wt. of header = 22.6 kg)	18.5
Conductor Height (cm)	1.27
Conductor Thickness (cm)	.23
Overall Conductor Length (meters)	4.57
Inductance L_o w/o Contact (μh)	7.13
Inductance with Contact L_c (μh)	4.64
Inductance Ratio L_o/L_c	1.54

240 μf @ 10 kv (12,000 joules)

Risetime w/o Contact τ_r^o (μsec)	71.0
Risetime with Contact τ_r^c (μsec)	40.5
Peak Field w/o Contact B_o (kOe)	48.6
Peak Field with Contact B_c (kOe)	144.0
Compression Ratio B_c/B_o	2.96
Peak Current I_p^o (ka)	58.0
Peak Current I_p^c (ka)	72.10
Peak Current Ratio I_p^c / I_p^o	1.24
Input Energy E_m^o (kj)	11.99
Input Energy E_m^c (kj)	11.37

400 μf @ 10 kv (20,000 joules) Extrapolated Parameters

B_o (kOe)	63.4
B_c (kOe)	188
τ_r^c (μsec)	52
I_p (ka)	94.7

B) 240 KILOJOULE DEVICE

The engineering and design of a magnetically driven hammer for a maximum input capacity of 240 kilojoules was based primarily upon the experimental results obtained during the testing of the previously constructed 20 kilojoule device.

For a system which would be capable of operating with this magnitude of input energy, it was necessary to carefully calculate the basic electric and magnetic parameters of the system. The primary objectives of the design were aimed at minimizing electrical, magnetic and thermal stresses in the device.

The requirement that the device handle a maximum voltage of 20 kilovolts necessitated a careful examination with regard to potential breakdown points in the unit. It was determined that the major points of concern in considering effective insulating procedures were the input plate in the area of the center conducting tubes, the conducting tubes themselves, and the coil contact pieces. The insulating procedures designed for these areas of potential breakdown are considered effective up to 25 kilovolts, thus assuring safe operation at the required voltage level.

The primary concern in the design of the 240 kilojoule device was the distribution of the magnetic stresses in the coil body. From previous

experimentation with similar magnetic forming devices[2], it was found that a coil of approximately 13 cm radius produced a peak magnetic field in contact with a work piece, B_c (r), of $\approx$ 70 kilogauss at an energy input of 12 kilojoules. If we then extrapolate the field of this coil to an energy input of 240 kilojoules by the relationship

$$B_2 = B_1 (W_2 / W_1)^{1/2} \qquad (19)$$

$$= 70 \text{ kgauss } (240/12)^{1/2}$$

we will obtain a peak field value of $\approx$ 300 kilogauss. This field, comparable to 5.0×10^4 psi, would create an excessive stress on the coil body in the region between the work piece and the current conducting turns. The continual application of such extreme magnetic pressure would tend to create a progressive displacement of the conducting turns from the coil face and a consequent voltage breakdown. For this reason, it was necessary to change the coil geometry in such a way as to reduce these expected high magnetic fields. We have achieved this reduction by increasing both the coil radius and conductor height. In doing so, we have brought the projected peak magnetic field strength down to a value given by the relationship

$$B_2 \approx B_1 (R_1 / R_2)(h_1 / h_2) \qquad (20)$$

$$\approx (300 \text{ kgauss})(12 \text{ cm}/20 \text{ cm})(1.27 \text{ cm}/1.91 \text{ cm})$$

$$\approx 120 \text{ kgauss}$$

This reduced value of the magnetic field by a revision of the coil geometry essentially alleviates the condition of extreme stress in these regions of the coil.

The high energy which is absorbed in the resistive heating of the conductor during the discharge cycle results in a large incremental temperature rise above the steady state conditions. The magnitude of this increase may be determined by utilizing the relevant parameters obtained from the experimental evaluation of the device. In consideration of a characteristic surface temperature rise[3] over a half cycle of the magnetic field B_c, we may develop the relationship

$$T_c \approx (0.7)\ 3000\ B_c^2 \qquad \text{degrees/megagauss} \qquad (21)$$

The observed peak magnetic field in the 240 kilojoule device for the normalized operation at 2400 μf, 20 kv was 190 kOe. Inserting this value in the above equation we obtain an incremental temperature rise $\Delta T \approx 72°C$.

An important factor in the thermal consideration is the underwater operation of the device. This will permit the coil shell to act as an efficient heat sink for the joule losses in the conductor. In connection with this situation the cross-sectional area of the contact piece between the coil shell and outer conductor was designed on the order of 3 to 5 times that of the conductor, thus permitting maximum thermal conductivity.

The basic parameters of the 240 kilojoule device are presented in the table below:

TABLE IV

BASIC PARAMETERS OF 240 KILOJOULE DEVICE

Nominal Radius (cm)	25.4
Conductor Radius (cm)	20.0
Number of Turns	17
Weight (kg)	160
Conductor Height (cm)	1.91
Conductor Thickness (cm)	0.95
Overall Conductor Length (cm)	1340
Inductance L_o w/o Contact (μh)	34.0
Inductance L_c with Contact (μh)	6.6
Inductance Ratio L_o/L_c	5.2

2.40 mf @ 20 kv (240,000 joules)

Risetime w/o Contact τ_r^o (μsec)	450
Risetime with Contact τ_r^c (μsec)	180
Peak Field w/o Contact B_o (kOe)	33
Peak Field with Contact B_c (kOe)	190
Compression Ratio B_c/B_o	5.75
Peak Current I_p^o (ka)	167
Peak Current I_p^c (ka)	380
Peak Current Ratio I_p^c/I_p^o	2.27

The conductor material selected for the 240 kilojoule device was beryllium copper (Be Cu), alloy #10. Its chemical composition is given in Table V and the relevant properties are presented in Table VI.

TABLE V

Element	% Composition
Beryllium	0.40 - 0.70
Cobalt	2.35 - 2.70
Copper	Balance

TABLE VI

Property	BeCu #10
Tensile Strength (psi)	120×10^3
Specific Heat (cal/cm^3-°C)	0.875
Resistivity (ohm-cm)	3.03×10^{-6}
For 240 Kilojoule Device	
Transient Temp. Rise ΔT (°C)	72°C

The conducting bar was machined from a solid block of BeCu. This operation eliminated the need for soldered joints and thus removed a potential cause of voltage breakdown.

In Figs. 5 and 6 are illustrated the magnetic field profiles for the 240 kilojoule device in both the contact and non-contact modes.

IV) EXPERIMENTAL RESULTS

The experimental measurements which were undertaken during the initial phase of the contractual period were oriented toward the investigation of the sonic field which is generated and propagated in the liquid medium by the high energy pulsed discharge into a high field magnetic coil. The observation of this acoustic pulse was carried out by the utilization of a piezoelectric transducer system, the development of which has been discussed in Chapter II of this Summary Report.

A) PRESSURE STUDIES

The initial investigations of the pressure pulse were made possible by the employment of a previously developed high field magnetic device which will hereafter be referred to as Hammer I-B. The geometric and electromagnetic characteristics of this device are listed in Table VII.

TABLE VII

Coil Radius, R_o, (cm)	5.0
Conductor Height (cm)	1.3
Inductance in Contact with Work L_c (μh)	1.1
@ 150 μf (7.5×10^3 joules) 10 kv	
Risetime in Contact with work τ_r^c (μsec)	22
Peak Field in Contact with work B_r^c (kOe)	260

The apparatus for the observation of the acoustic pressure pulse in the liquid medium consisted of the transducer system, T-1, and an oscilloscope for the recording of the integrated voltage signal generated in the Ba T_i O_3 crystal. A metallic diaphragm was placed against the face of the coil and, at the time of the pulsed discharge of the current, was thrust away from the face by the magnetic field generated in the coil. The plate traveled on supporting rods to insure the formation of a plane wave parallel to the coil face. A schematic illustration of the experimental setup is presented in Fig. 7.

1) Sonic Field Investigation

The transducer system, T-1, was used to probe the sonic pressure pulse in both the radial and normal directions with respect to the coil face. The investigation was carried out on various time scales. In accordance with this effort it was observed that two distinct pressure peaks existed at different points in time. The first observed pressure pulse (hereafter referred to as the Type I wave) appeared at a time interval consonant with the velocity of sound in water ($\sim$ 1500 m/sec) for a given normal distance, D_n. The second pressure pulse (referred to as the Type II wave) had a characteristic velocity of $\sim$ 400 m/sec. The measurements obtained from the pressure transducer are presented in the following illustrations. Figure 8 shows the pressure profile of

the Type I pulse. The data for these observations were taken with an energy discharge of 300 joules. This graph illustrates the variation of pressure with vertical or normal distance, D_n, from the plate to transducer tip and also the variation with radial distance from the center of the coil, D_r. Figure 9 illustrates the Type II pressure pulse at the same energy level.

The analysis of the observed data has led to a determination as to the behavior of the liquid medium when subjected to the action of the pulsed magnetic field and the resultant thrust of the diaphragm away from the coil face. The slow Type II wave can be associated with the mass flow of the medium upon its displacement from the equilibrium state by the action of the diaphragm. This mass propagates into 2π space with a symmetrical radial flow. The Type I wave is propagated initially as a plane progressive wave with high velocity particle displacement. A further understanding of the two distinct types of pressure pulses was carried out by the introduction of the following useful observational method.

2) Photographic Techniques and Analysis

High speed photographic techniques have been employed to observe the displacement of the diaphragm (driver plate) from the coil

face. In the operational mode under present consideration the thrust of the driver plate is not restricted in any way except for the frictional effects on the supporting rods. These effects have been minimized by the use of nylon bushings on the rods.

a) Experimental Setup

The high-speed photographic techniques used to observe the phenomenon of plate movement involved the following equipment: a General Radio Type 1531-A electronic stroboscope is used in conjunction with a Rutherford Model B7B delay generator. At the time of the capacitor discharge, a synchronized output pulse is obtained from the capacitor bank. This pulse is then fed into the delay generator and delayed from 0 to 10 msec before going to the stroboscope. The stroboscope is operated on a single flash mode with a flash duration of 3 μsec. The time delay is checked on a Tektronix oscilloscope. In this manner, the motion of the driver plate can be "stopped" and we can photograph it at different positions corresponding to the time delay. A schematic of the experimental setup is shown in Fig. 11.

b) Analysis of Results

The photographic techniques utilized in this phase of the experiment have enabled the observation of cavitation on the surface of the driver plate after the discharge. This formation of bubbles, or voids, in the liquid medium occurs whenever the pressure on the parts of a body moving in that medium is reduced so low by the inability of the flow to follow the surface that a near vacuum is produced. Thus, diaphragms having large accelerations and therefore pressure reductions on the surfaces will cavitate readily. In our situation, when the capacitor bank is discharged, the plate attempts to move upward but such movement is restricted by the large mass of water over it. As a result, the plate tends to push the water out of the way and this mass flow is primarily in the radial direction. The velocity in this direction reduces the pressure on the surface of the diaphragm resulting in the production of the observed voids. As the plate tends to move toward this low pressure area it creates behind it another low pressure area which retards its forward motion. The production of the alternating low pressure areas results in oscillations of the plate while close to the coil face. This oscillatory

motion of the driver is very fast in the beginning of the cycle but tends to slow down and stop as the cycle progresses. This is verified by noting the absence of cavitation after 900 μsec. The flow of the water is then able to follow the surfaces of the plate and no low pressure areas are created. A photograph of the coil and driver plate showing cavitation at a particular point in time is illustrated in Fig. 10.

The number of voids/mm^2 projected in the plane of the viewing area above the plate versus the time interval after the discharge of the bank is shown in Fig. 12. A high intensity noise pickup was noted on the crystal response oscillograms between the time of the Type I and Type II pressure pulses. This noise was due primarily to the collapse of the voids releasing the energy with which they were created.

3) Channeling of Acoustic Pressure Pulse

The initial pressure studies were conducted in such a fashion as to permit a 2π propagation of the pulse with a consequent decrease in the energy density of the pressure wave. In order to maintain the intensity of the generated pulse for as long a period as possible, the

effect of channeling the flow was investigated. The channeling device utilized was an aluminum cylinder, one foot in length, with an inside diameter of 6". A clearance of 1/16" on the radius was maintained between the driver plate perimeter and cylinder inner wall.

With the employment of this device, it was possible to delay the radial expansion of the pressure pulse. The effectiveness of the channeling device is observable in the following table which compares the pressure slopes for variable input energy.

TABLE VIII

Operational Mode	$a_1 = P_I/E$ (atm/kj)	$a_2 = P_{II}/E$ (atm/kj)
Unchanneled	60	90
Channeled	75	75

From the table we observe that the channeling of the acoustic pulse increases the pressure of the Type I wave over the unchanneled mode. For the Type II wave with which we associate the phenomenon of mass flow, there is a decrease of the maximum pressure obtained in the channeled mode. The reason for this somewhat anomalous effect is the apparent decrease in plate acceleration due to the absence of the

radial flow. With the slower movement of the plate the intensity of the mass flow wave is greatly decreased.

Having noted the pressure increase for the Type I wave in the channeled mode, further measurements were conducted to delineate the relative merits of the two distinct types by the employment of the following experimental method.

4) Suppression of Driver Plate Movement

In an earlier part of this report (cf. IV-A-1), an explanation of the behavior of the two wave types was made. The Type I wave was initially identified as an acoustic wave with high velocity particle displacement. The Type II wave was associated with the mass flow of the liquid and movement of the diaphragm.

The experimental measurements under consideration here involved the suppression of driver plate movement by bolting this device to the face of the Hammer I-B coil. In this manner, the elimination of the Type II pressure wave was effected. Figure 13 illustrates the pressure measurements which have been obtained by the employment of the above method. The most significant observation is the decrease in the amplitude of the Type II wave in the suppressed mode of operation. The pressure slope for the mass flow wave (P_{II}/E) is reduced by a factor of 2 over the unsuppressed mode. In the restriction of the driver

plate movement we do not observe the complete absence of pressure due to the Type II wave since the bolting of the diaphragm on its perimeter still permits some movement at the center. At low energies such driver plate displacements appear to be elastic but for the higher energies we have noted inelastic deformations with magnitude dependent upon the energy level.

The Type I wave was investigated as a function of normal distance, D_n, from driver plate to transducer tip in both the unchanneled-suppressed and channeled-suppressed modes at a low energy level. The observed pressures are illustrated in Fig. 14.

The diaphragm thickness for the above measurements was maintained at 1/2". It was felt to be appropriate at this phase of the experimental study to investigate the dependence of pressure for the Type I wave on varying diaphragm geometries and material composition.

5) Driver Plate Studies

The investigation was conducted by utilizing diaphragms of an aluminum alloy and of copper. The relevant physical and electrical properties of these two materials are listed in Table IX on the following page.

TABLE IX

Properties	Aluminum 2024-T3	Copper
Electrical Conductivity (mho/meter)	1.76×10^{-7}	5.88×10^{-7}
Yield Strength (psi)	64×10^{3}	35×10^{3}
Density (gm/cm^3)	2.7	8.8

The thickness of the plates was allowed to vary between 0.005" and 0.500". The pressures which resulted from the employment of the aluminum diaphragms is presented in Fig. 15. The measurements were carried out at varying energy levels. An inspection of the data illustrates the interesting phenomenon of a pressure peak for a given driver thickness at each energy level. The point at which this peak occurs is quite near the electrical "skin depth" of the diaphragm. The skin depth of the aluminum plate, which is a function of the resistivity and and the frequency, amounts to approximately 0.046". The corresponding pressures resulting from the utilization of the copper diaphragms of varying thickness are illustrated in Fig. 16. The calculated skin depth for this material is 0.024".

It was thus evident from the above measurements that an optimization of the pressure for the Type I wave could be obtained with a driver plate thickness of, or near, the skin depth value for that material.

The observation of lower pressure values for the copper diaphragms may be explained by the comparatively low yield strength of that material. At the higher energies the elastic deformation of the plate in the suppressed mode utilized a large proportion of the applied energy with the consequent decrease in the high velocity particle displacement which is responsible for the propagation of the Type I wave.

B) DEFORMATION MEASUREMENT

The pressure studies which were conducted for the purpose of investigating the behavior of the acoustic pulse have been complemented by a detailed study of the effective forming capability of this pressure pulse.

1) Initial Studies

The hydromagnetic forming device, MFH-2, was utilized in the deformation measurements in conjunction with various mechanisms for the optimization of the forming effect. A description of the geometric and electromagnetic parameters of this device is presented in Table III of Chapter III-A.

The material utilized for the forming operation was the aluminum alloy 2024-T3 which is currently of importance in the development of aerospace hardware. Certain of the important properties of this material have been outlined in Table IX (page 30) of this Summary Report.

The initial studies of the forming capability were conducted in the liquid medium employing the 20 kilojoule device MFH-2. Measurements were obtained in both the unchanneled-suppressed and channeled-suppressed modes of operation. The restriction of the driver plate effectively negated the forming contribution of the Type II wave. Consequently, the plate deformations obtained resulted primarily from the action of the high velocity particle motion in the liquid medium associated with the Type I acoustic wave. Diaphragms of thicknesses 1/2" and 1/4" have been employed in these measurements in conjunction with a work piece thickness in the aluminum alloy of 0.040". The normal distance D_n for the unchanneled mode of operarion was 7 cm while for the channeled mode the normal distance was 24 cm. This variation in the distance from driver plate to work piece was necessitated by the length of the channeling device. Figure 17 illustrates the obtained deformation measurements for varying energy levels. The observed linear deformations obtained for the channeled mode are smaller than those obtained in the unchanneled mode. It is possible to normalize these measurements to a distance D_n of 7 cm by the utilization of the deformation attenuation graph of Fig. 26.

The relative efficiencies of Hammer I-B utilized for the initial pressure measurements and the hydromagnetic forming device MFH-2

have been compared in Fig. 18. The effective forming ability of each device is related to the peak magnetic pressure P_m for the given energy and capacitance level by the equation

$$P_m = (B_c^2/8\pi) \cdot (2W_B/C)^{1/2} \qquad (22)$$

where B_c is the peak magnetic field. The slope of each deformation-pressure graph is given in Fig. 18 in cm/atm. The device MFH-2 is observed to possess the greater forming capability of the two devices. A pertinent factor in this phenomenon was the variance of risetime to peak current in the two devices. The effect of the magnetic field duration on the hydromagnetic forming was investigated by the following series of measurements.

2) Field Duration Studies

Experiments have been conducted utilizing the hydromagnetic forming coil MFH-2 in conjunction with an energy discharge unit of variable capacitance. These studies were carried out in order to investigate the relationship of the forming process with an increase in the risetime, τ_r, of the current to its peak value. The dependence of the risetime on the capacitance is given by the equation

$$\tau_{r_1} \approx (C_1/C_0)^{1/2} \tau_{r_0} \qquad (23)$$

Five levels of bank capacitance were utilized in this phase of the experimental program giving risetimes in the region of 41 μsec

to 58 μsec. An observable increase in linear deformation was noted in this range.

The investigation was carried out at three energy levels. Figure 19 illustrates the relationships obtained for both the 1/2" and 1/4" driver plates in the unchanneled-suppressed mode. In the following Table X, the slope of the deformation increase with variable risetime, $dD/d\tau_r$, as a function of both energy level and driver plate thickness is presented.

TABLE X

DEFORMATION SLOPE
($dD/d\tau_r$ cm/μsec)

	1/2" Driver	1/4" Driver
4.32 kj	4.12×10^{-3}	2.65×10^{-3}
5.88 kj	5.43×10^{-3}	4.12×10^{-3}
7.68 kj	8.85×10^{-3}	3.53×10^{-3}

The observation of the data obtained in this phase of the experiment illustrates a linear increase of deformation with the addition of capacitance and the consequent rise in the magnetic field duration. We have earlier noted the pressure dependence upon the driver plate thickness. As the diaphragm geometry approached the optimum

condition of skin depth thickness, the effective forming ability increased. The approach in this later phase of the experimental program has been to hold the driver plate geometry constant and to increase the electrical skin depth δ from the relationship

$$\delta = (1/\pi)(\rho\tau_r/10^{-7})^{1/2} \qquad (24)$$

where ρ is the electrical resistivity of the material. We are then, in essence, optimizing the deformation by having the value of δ approach the driver plate thickness. The projected deformations corresponding to a risetime of 100 μsec (C_B = 1500 μf) are also illustrated in Fig. 19. As the skin depth approaches the diaphragm thickness there will be a sharp decrease in the effective forming capability due to the field diffusion through the plate.

The above investigations with regard to the duration of the magnetic field pulse have led to the consideration of the phenomenon of overdamped energy discharge, which is discussed in the following section.

3) Crowbar Circuitry

We show here that, for a given energy input into a hammer coil, more thrust against a metal driver plate is generally developed by using crow-barred operation.

We have considered first the case where the driver plate is thick compared with the skin depth. The rate of energy loss due to resistivity is given approximately by the rate of magnetic field diffusion into the metal. For the crow-barred case the skin depth is (in appropriate units of resistivity η):

$$S_c = \sqrt{\eta t} \tag{25}$$

so that the power dissipation per unit area of the driver plate is

$$P_c = (B^2/8\pi)(dS_c/dt) = (B^2/8\pi)(S_c/2t) \tag{26}$$

For oscillatory operation, with half-period τ, the skin depth remains constant at $S_o = \sqrt{\eta \tau}$, and the power dissipation is

$$P_o = (B^2/8\pi)(S_o/\tau) \tag{27}$$

The ratio of power dissipation is then

$$P_o/P_c = 2t/\tau \tag{28}$$

If the half-cycle time τ is short compared with the crow-barred decay time, ther $P_o \gg P_c$, and there is needlessly rapid decay of the magnetic pressure in the oscillatory operation.

We consider now the case where the driver plate is thin compared with the skin depth. Then the driver plate behaves like a fixed resistance. The time for decay of the induced current in the driver plate is the L/R-time, which is

$$\tau_R = ab/\eta \tag{29}$$

Here a is the thickness of the driver plate and b is the depth of the flux-reservoir, i.e. roughly the distance between the driver plate and the mean current path in the hammer.

In crow-barred operation there is only one brief thrust, of duration τ_R. In oscillatory operation, the first quarter-cycle dissipates exactly the same amount of energy as does the crow-barred operation and delivers the same thrust. Now, however, there are additional thrusts on subsequent half-cycles. In this case, oscillatory operation is preferable.

Since we were able to select the driver-plate thickness so as to minimize the thrust for a given input energy, we chose a plate at least as thick as the skin depth, and therefore, crow-barred operation will generally be more effective than oscillatory operation.

a) Crowbarring in Air

Experiments were conducted in air with varying work pieces to determine the effectiveness of the crow-barring operation. The 20 kilojoule forming device, MFH-2, was utilized for these measurements. The investigation seemed to indicate that the crow-barring in air produced insignificant increases in deformation for the workpiece thicknesses under consideration. An illustration of the deformations obtained as a result of these

initial experiments in Fig. 20. A schematic of the circuitry is given in Fig. 21.

b) Crowbarring in the Hydromagnetic Mode

Measurements have been obtained in the hydromagnetic mode which utilize a crowbar circuitry rather than the normal oscillatory response of the pulsed current. It was noted above that no sizeable increase in deformation was obtainable by the overdamping of the capacitor discharge for the case of magnetic forming in air. An attempt was then made to test further the crowbar circuitry by employing it in the underwater mode. The time at which crow-barring occurred, τ_{cr}, was determined from an operational relationship for the present experiment with $\tau_{cr} \approx 1.1\,\tau_r$. For the case of MFH-2, with $\tau_r = 41$ μsec, we obtained a value of $\tau_{cr} \approx 45$ μsec.

In the hydromagnetic mode, the crowbar circuitry was utilized at three energy levels. The measurements were obtained in the unchanneled-suppressed condition with the 1/2" driver plate and with bank capacitance of 240 μf. In addition, varying work piece thicknesses were employed. An illustration of the observed data is presented in Fig. 22. It appeared from these values relating the oscillatory and crow-barred modes that an observable increase of deformation does exist at the higher energies.

4) Attenuation of Deformation

A mechanism was developed which permitted the measurement of the fall-off of forming ability with increasing normal distance D_n of diaphragm to workpiece, w_p. A schematic of the equipment utilized in this phase of the experimental program is illustrated in Fig. 23. Studies were conducted in two operational modes.

a) Unchanneled Mode

Measurements have been carried out in the unchanneled-suppressed mode utilizing the 1/2" driver plate at a variable normal distance from plate to work piece. The observation of the data obtained from this phase of the experiment has indicated an exponential fall-off of deformation with decreasing normal distance. This phenomenon of deformation attenuation correlates well with the earlier studies involving pressure as a function of increasing normal distance with the Hammer I-B magnetic forming coil. An illustration relating the linear deformation and normal distance D_n is given in Fig. 24.

Of equal interest is the observed attenuation of the volume deformation as presented in Fig. 25. Investigations of the data have indicated a close correspondence with the exponential fall-off of the linear deformation.

b) Channeled Mode

The measurement of the attenuation of deformation was extended to the channeled operational mode. In this case, the propagation of the Type I wave was confined by the cylindrical walls of the channeling device. The acoustic intensity of the sonic wave is preserved by the minimizing of radial expansion. A linear attenuation of effective forming ability with increasing normal distance is noted in this mode. Figure 26 illustrates the observed fall-off of linear deformation. The attenuation of the volume deformation is presented in Fig. 27.

5) Concentration of Pressure Pulse

Concentrating devices have been designed and utilized for the purpose of multiplying the energy density of the acoustic wave and thus increasing the acoustic intensity.

a) Initial Studies

In order to examine the effects of increasing the energy density of the acoustic pressure pulse, a concentration device was constructed from a stainless steel sheet 0.050" thick. The sheet was rolled into the form of a truncated cone with an opening of 2" diameter at the top and a 6" diameter opening at the bottom. The wall of the cone was at an angle of 66° with respect to the

driver plate. The concentrator was then probed with the transducer T-1 in a normal direction from the coil to determine any possible improvement of the pressure pulse. Figure 28 illustrates the peak pressures obtained for a variable normal distance D_n. Reference to Fig. 14 indicates that an increase of $\sim$ 10% is obtained above the unchanneled-suppressed mode. Investigations were conducted to determine reasons for this minute increase in peak pressure observations. The transducer was employed in probing the pressure field outside the concentrator wall. It was found that the wall thickness of the concentrating device was insufficient to prevent almost total refraction of the pressure front with the consequence that the mechanism exerted little effect on the propagating sonic pulse. As a result of these observations, a system of adequate thickness was designed and employed for use in the following investigations.

b) Optimization of Pulse Concentration

A second device for the intensification of the acoustic pressure wave was constructed. The average wall thickness of this system was made large to preclude the possibility of extreme refraction of the pressure pulse at the concentrator wall. A

schematic illustration of the device is presented in Fig. 29. The system was initially constructed as a series of decreasing cylindrical diameters from an initial section diameter of 9.75" to a final section diameter of 3" in six sections. The driver plate to work piece distance D_n in the utilization of all sections was 34 cm. Measurements were obtained at varying energy levels with a suppressed 1/2" diaphragm. An illustration of the deformations obtained is presented in Fig. 30. A nonlinear increase in deformation at the 12 kilojoule level is noted.

Studies were conducted to investigate further the effective forming ability of the concentrator apparatus by the removal of various sections, thus decreasing the normal distance D_n. The data obtained for four cases of section removal at varying energy levels are presented in Fig. 31. A decreasing of forming ability is noted for increasing D_n. It thus appears that optimization of the deformation occurs for the minimization of the step-to-step ratio of the cylindrical diameters with a consequent maximum deformation for the concentrator suppressed mode in the completely conical geometry.

The interior of the device was machined to permit utilization

of the above geometry. An increase of ~ 25% in linear deformation was noted with the employment of the optimized system. An illustration of the results obtained in the conical geometry is presented in Fig. 32.

6) Driver Plate Modification

The utilization of the aluminum diaphragms at high energy levels in the suppressed mode resulted in substantial deformations to the plates. The necessity of continually changing the driver plates after each high energy shot has been avoided by the development of a high tensile strength diaphragm. The device to be employed was a combination of stainless steel and copper for high conductivity. The relevant properties of these materials together with the same properties for aluminum are presented in Table XI.

TABLE XI

	Al 2024-T3	Stainless Steel	Copper
10^3 psi Yield Strength	64	175	35
Electrical Conductivity 10^7 mho/meter	1.70	0.15	5.65

The copper insert was made thicker than the skin depth in order to insure maximum conductivity in the modified diaphragm. Initial experi-

mentation with the device at high energy levels demonstrated a deformation increase $\approx$ 16% over the similar shot with an aluminum driver plate.

7) Confined Mode

In order to obtain a "hydraulic piston" effect in the hydromagnetic pressure studies a device with completely confined geometry was constructed. A schematic of the device is given in Fig. 33. The utilization of this device at the low values of normal distance D_n resulted in the measurements which are illustrated in Fig. 34.

The studies in the confined mode were obtained with both the unsuppressed and suppressed diaphragms. No significant variation of deformation was noted between the two cases.

a) Variation of Die Diameter

In order to investigate the effect of variation of die diameter on the forming ability of the hydromagnetic pulse, a modification of the vacuum die in the confined suppressed mode was carried out. Initial observations indicated a linear relationship between the obtained deformations and die diameter as illustrated in Fig. 35.

V) 50 KILOJOULE INDUCTIVE STORAGE SYSTEM

A) DESIGN CONSIDERATIONS OF STORAGE COIL

The inductive storage coil was designed with a Brooks configuration to achieve highest inductance for a given length of conductor. After studying various fabrication techniques aluminum ribbon was chosen as the conductor material. The purpose of this choice was threefold:

1) Ribbon material is rigid enough so that a coil constructed with this material to a reasonable radial thickness would require no winding form.
2) It is relatively easy to increase the conductor cross-section in order to reduce power consumption with a strip type.
3) Very high packing densities can be achieved in coils that are wound with ribbon conductors.

Inductance of the coil is given by

$$L = 2.6 \times 10^{-8} b N^2 \text{ henry}$$

where b is the height of the coil and N is the total number of turns. The DC charging power of this coil is given by

$$P = 7.3 \times 10^{8} \rho E / b^2 \quad \text{watts}$$

where ρ is the resistivity of the conductor material in ohm-cm, E is the stored energy in joules.

The coil was designed to store 50 kilojoules with 5000 amps at room temperature with a power requirement of 15 kw. This power requirement fixes the coil height, b, at 14 cm. Consequently, 105 turns are required to give the desired inductance. The design parameters of the coil are given in Table XII on the following page.

The coil was constructed with these design parameters and was divided into five sections for current multiplication purposes.

B) MEASUREMENT OF ELECTRICAL PARAMETERS

Series inductance of the package was measured to be 3.93 mh. Parallel inductance, however, is lower than anticipated (80 μh). Series resistance is slightly higher than anticipated (29 mΩ). The coil is insulated to 18 kv from turn-to-turn. An overall 89% mean packing density was achieved (maximum 90%), which shows the degree of efficiency that can be obtained with this configuration. The sections of the coil were connected to the appropriate switches with a number of parallel flexible cables to reduce resistance and inductance. Materials used (stainless steel, aluminum, mylar and phenolic) have adequate properties to withstand the strains developed and have very high corrosion resistances.

TABLE XII

	DESIGN PARAMETERS	MEASURED PARAMETERS
Material	Aluminum Ribbon	
L	4 mh	3.95 mh
R	20 mΩ (room temp.) 2 mΩ (LN temp.)	29 mΩ (room temp.) 2.9 mΩ (LN temp. anticipated)
N	105 turns	
Conductor Thickness	.132 cm (.053")	
Total Length	140 cm (460 ft.)	
b = c	14 cm	
a	21 cm	
Weight of Coil	153 lbs.	------
Total Weight	-------	------
Power Requirement	2750 amps, 6v, 15 kw at LN temperature	2750 amps, 8v, 22 kw at LN temperature
Cool Down	80 - 100 liters LN	
Energy Storage Density	50 joules/lb	

C) CURRENT MULTIPLIER SWITCH

The current multiplier switch incorporated into the 50 kilojoule inductive storage system actually consists of two separate switching stages. Both are magnetically actuated, being driven by high current discharge into 12 μh driver coils. The fields produced act on aluminum driver plates which are attached to the movable switching elements. Both switches use mercury pool and mercury-wetted copper electrodes for good electrical contact.

The interrupter switch, SS15-1, is composed of the base plate and driver coil which are potted in epoxy, the movable interrupter element, guide rods and a can which seals off the switch for pressurization of up to 10 c nospheres to suppress arcing (see Figure 36(a)). During the charging of the inductor this switch is closed and the coil sections are in series electrical connection. Upon firing, the interrupter element is forced up with the guide rods maintaining a vertical and irrotational motion. Upon reaching an energy-dependent maximum height, the element slides back down the guide rods, resetting itself upon reaching the bottom.

The maker or closure switch (see Fig. 36(b)), which, during charging is in the open (raised) position, when fired drops down and connects the load in parallel with the five coil sections. Connections to the load come directly from the movable closing element so as to keep the number of

mercury pool contacts to a minimum. This closing element must be manually reset (raised) after each switch operation.

It is imperative, due to efficiency considerations, that the closure switch makes contact before the SS15-1 begins interruption since large amounts of energy would be lost trying to place the charged inductor in an open circuit.

The driver coils can be fired from the same capacitor bank, and can be connected either in series or in parallel, depending upon the capacitance used. The coils could also be fired separately with individual capacitor banks and separate trigger units. The driver coils have each been tested to energies of 1.5 kj. Consequently, caution should be exercised in any attempt to drive them at higher energies.

The driver plates have been optimized with respect to electrical skin depth for capacitor banks of 100 μf when fired in parallel, 50 μf each when fired separately and 25 μf when fired in series.

D) EXPERIMENTAL MEASUREMENTS WITH THE STORAGE SYSTEM

All testing of the 50 kj inductive storage system has been done by means of capacitive charging and has been limited to < 12 kj (240 μf - 10 kv). In the system which involves the capacitive mode of operation, crowbarring of the capacitors occurs when maximum current is flowing and before the switching process begins. The one turn loop in the core of the storage inductor was

used for voltage, ringing times and current determinations during capacitive charging.

Figures 37(a), (b), (c) and (d) show schematic diagrams of the experimental circuit during four different steps of operation.

Figures 38 and 39 illustrate the voltage developed across equal resistances, one in the charging and crowbar circuit (series configuration) and the other in the parallel circuit. Charging of the inductor was achieved by a 800 μf capacitor bank at 1.5 kv. At peak current (~ 650 amp) an ignitron trigger circuit removes the capacitors and we are left with a simple LR circuit. The upper traces are from the series circuit and the lower traces are from the parallel circuit.

In Fig. 38 switching was not attempted. The current rises to maximum by capacitive charging and then decays due to internal resistance through the crowbar circuit. In the lower trace, the resistance (load) was not connected to the coil at any time although high transients are seen which are due to the rapidly changing magnetic field produced by charging the storage inductor.

With perfect switching we would expect the lower trace to climb to five times the voltage of the upper trace. From Fig. 39 the voltage, just before switching, is .675 volts. Therefore, 100% efficiency would be 3.38 volts after switching. From the lower trace of Fig. 39 we have

2.72 volts, or (2.72/3.38) • 100 = 80.5% efficiency.

Having the switching occur at the time of crow-barring is highly desirable so as to reduce losses due to LR decay. This is merely a matter of timing the firing sequence properly and depends mainly upon the energy used to drive the switching elements.

REFERENCES

1) W. G. Cady, Piezoelectricity, (Dover Publications, 1964).

2) "Research, Development and Manufacture of Magnetic Forming Coils," Advanced Kinetics, Inc., Contract NAS 8-11757 Final Report, March, 1965.

3) H. P. Furth, M. A. Levine, R. W. Waniek, Rev. Sci. Instr. 28, 949 (1947).

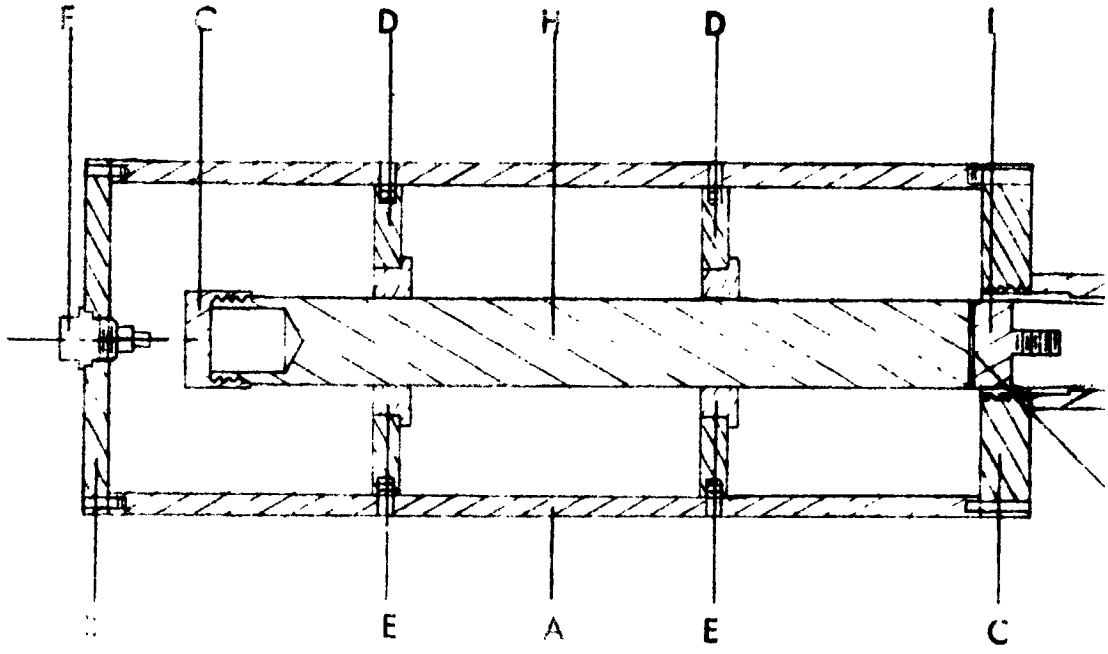

Fig. 1

PIEZOELECTRIC TRANSDUCER

TYPE #1

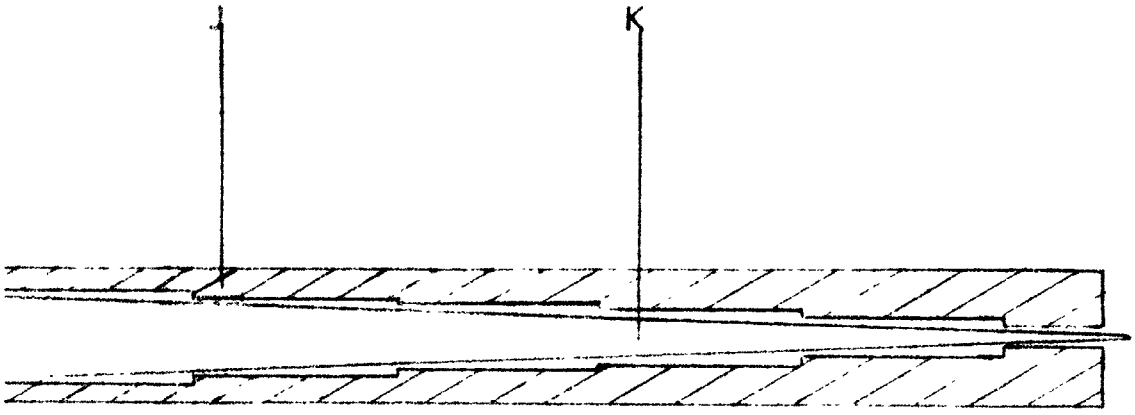

A - CYLINDRICAL HOUSING

B - REAR HOUSING COVER

C - FRONT HOUSING COVER

D - DELAY LINE SUPPORT

E - TEFLON BUSHING

F - BNC CONNECTOR

G - DELAY LINE CAP

H - ACOUSTIC DELAY LINE

I - TRANS.-DETECTOR CONNECTOR

J - TRANSFORMER SUPPORT TUBE

K - ACOUSTIC TRANSFORMER

L - PIEZOELECTRIC CRYSTAL

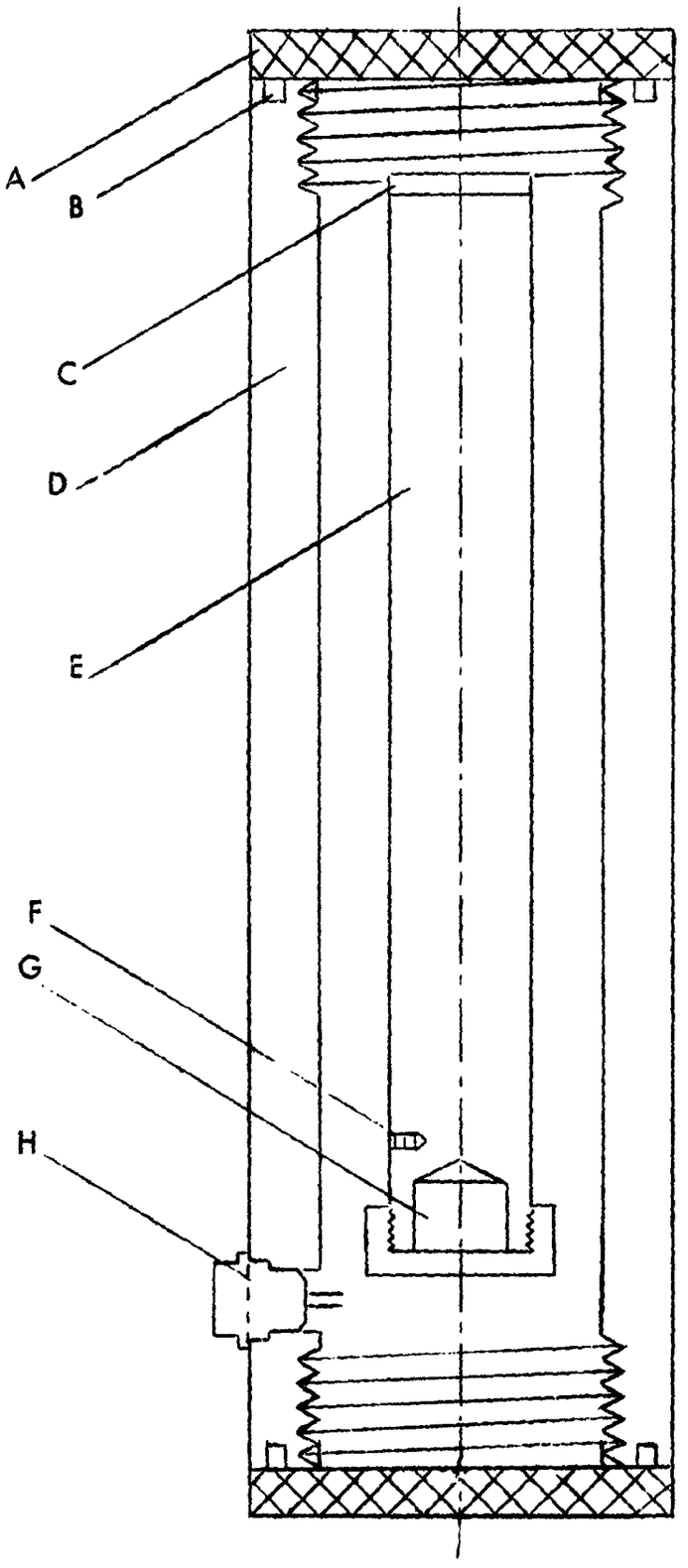

A - Transducer Cap (2)

B - O-Ring Groove (2)

C - Piezoelectric Crystal

D - Transducer Enclosure

E - Acoustic Delay Line

F - Signal Connection

G - Wave Dissipation Hole

H - BNC Connector

Fig. 2:
PIEZOELECTRIC TRANSDUCER

Fig. 3: MAGNETIC FIELD PROFILE FOR MFH-1

12 kj 240 μf

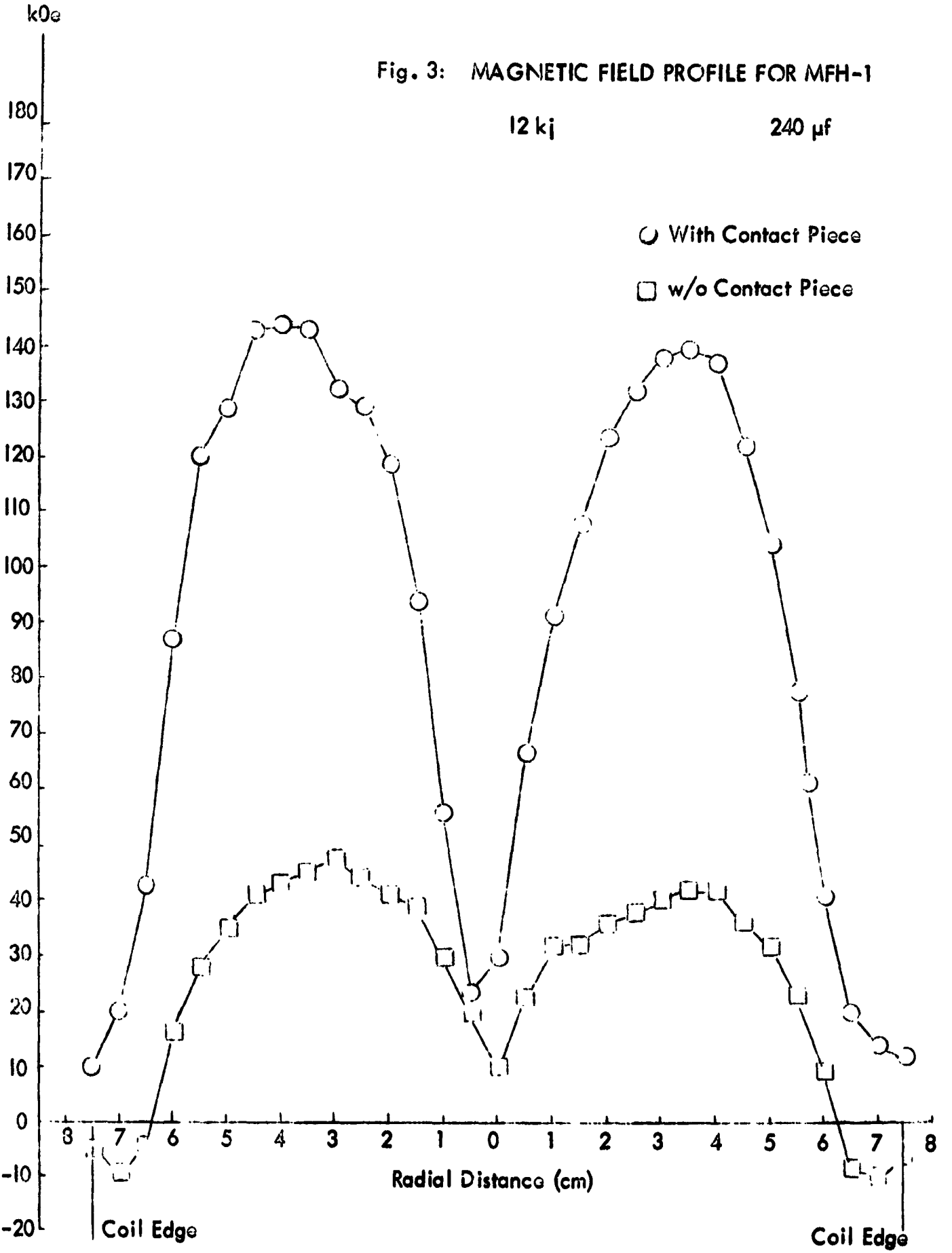

Fig. 4: MAGNETIC PRESSURE PROFILE FOR MFH-1

W_B = 12 kj

C_B = 240 μf

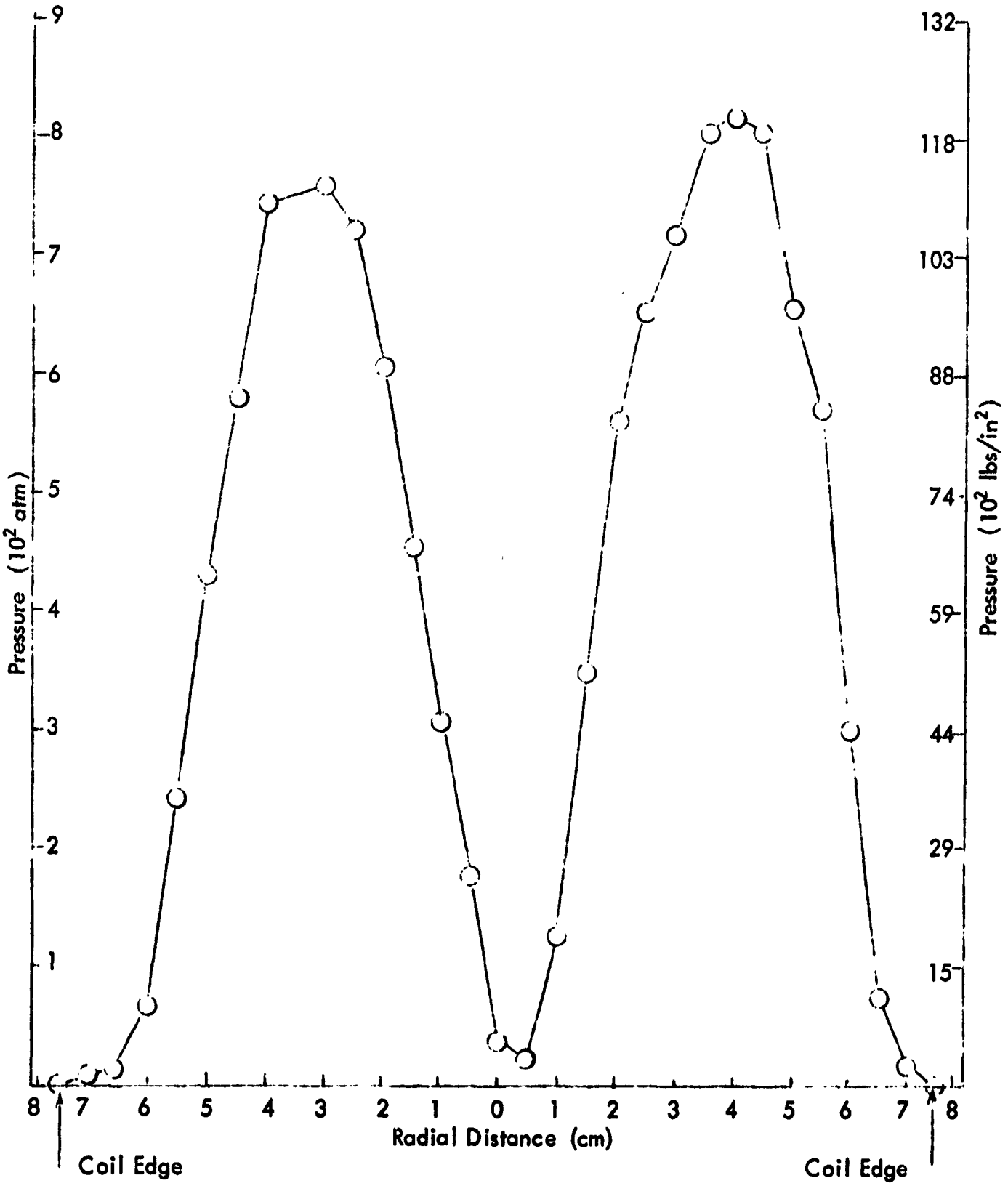

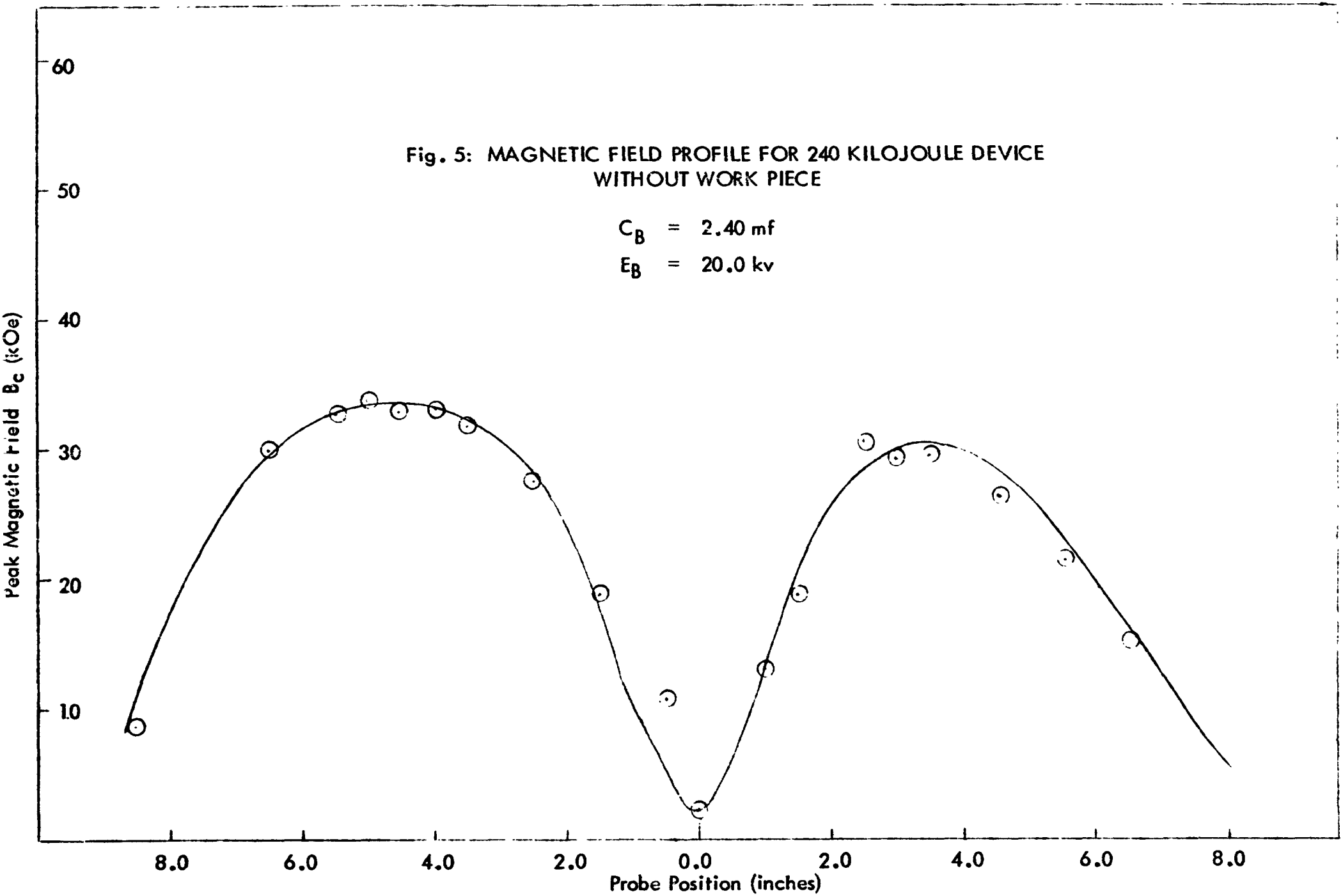

Fig. 5: MAGNETIC FIELD PROFILE FOR 240 KILOJOULE DEVICE WITHOUT WORK PIECE

C_B = 2.40 mf

E_B = 20.0 kv

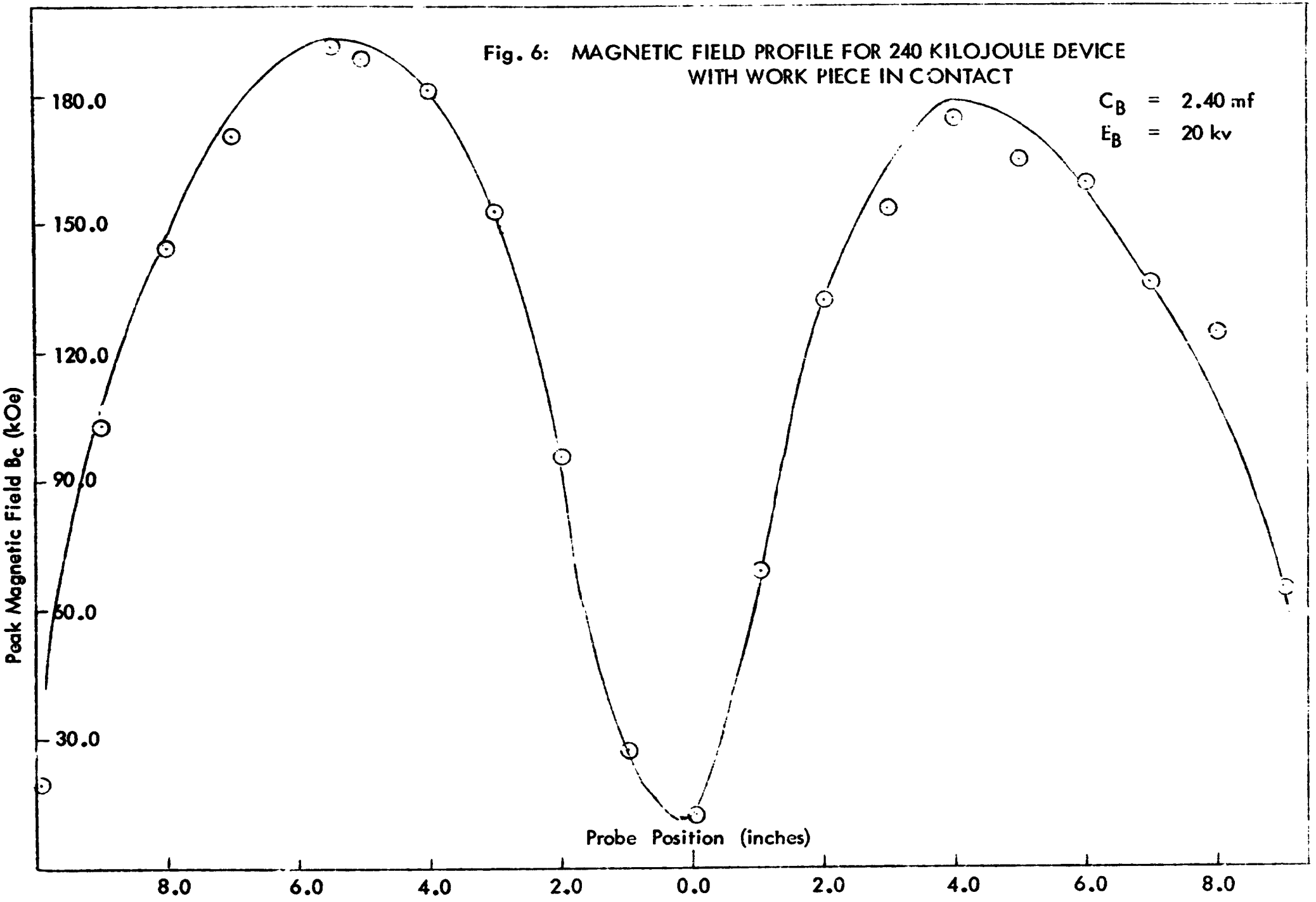
Fig. 6: MAGNETIC FIELD PROFILE FOR 240 KILOJOULE DEVICE WITH WORK PIECE IN CONTACT
C_B = 2.40 mf
E_B = 20 kv
Peak Magnetic Field Bc (kOe)
180.0
150.0
120.0
90.0
60.0
30.0
Probe Position (inches)
8.0
6.0
4.0
2.0
0.0
2.0
4.0
6.0
8.0

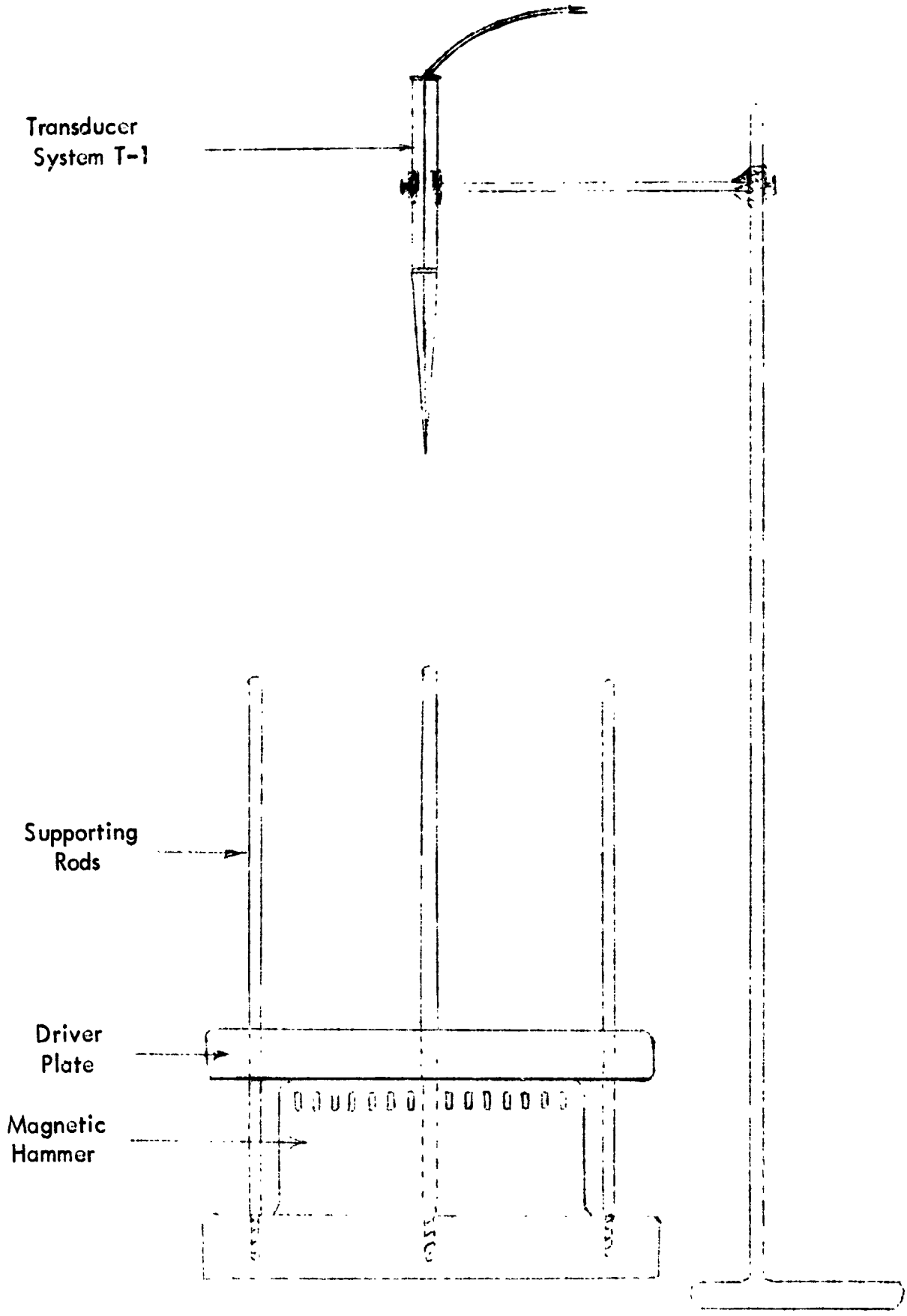

Fig. 7: SCHEMATIC ILLUSTRATION OF HAMMER I-B

Fig. 8: TYPE I PRESSURE WAVE PROFILE

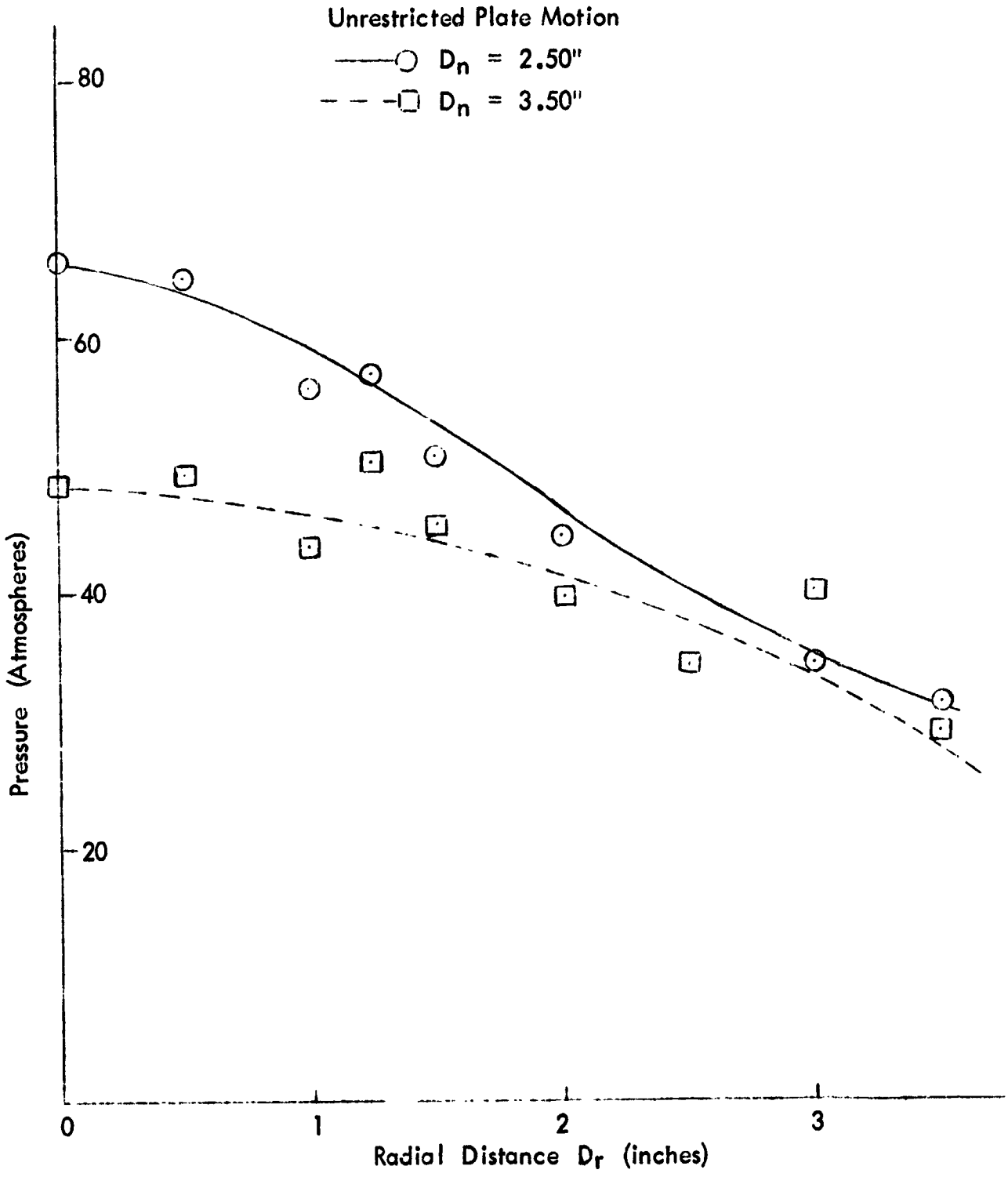

Fig. 9: TYPE II PRESSURE WAVE PROFILE

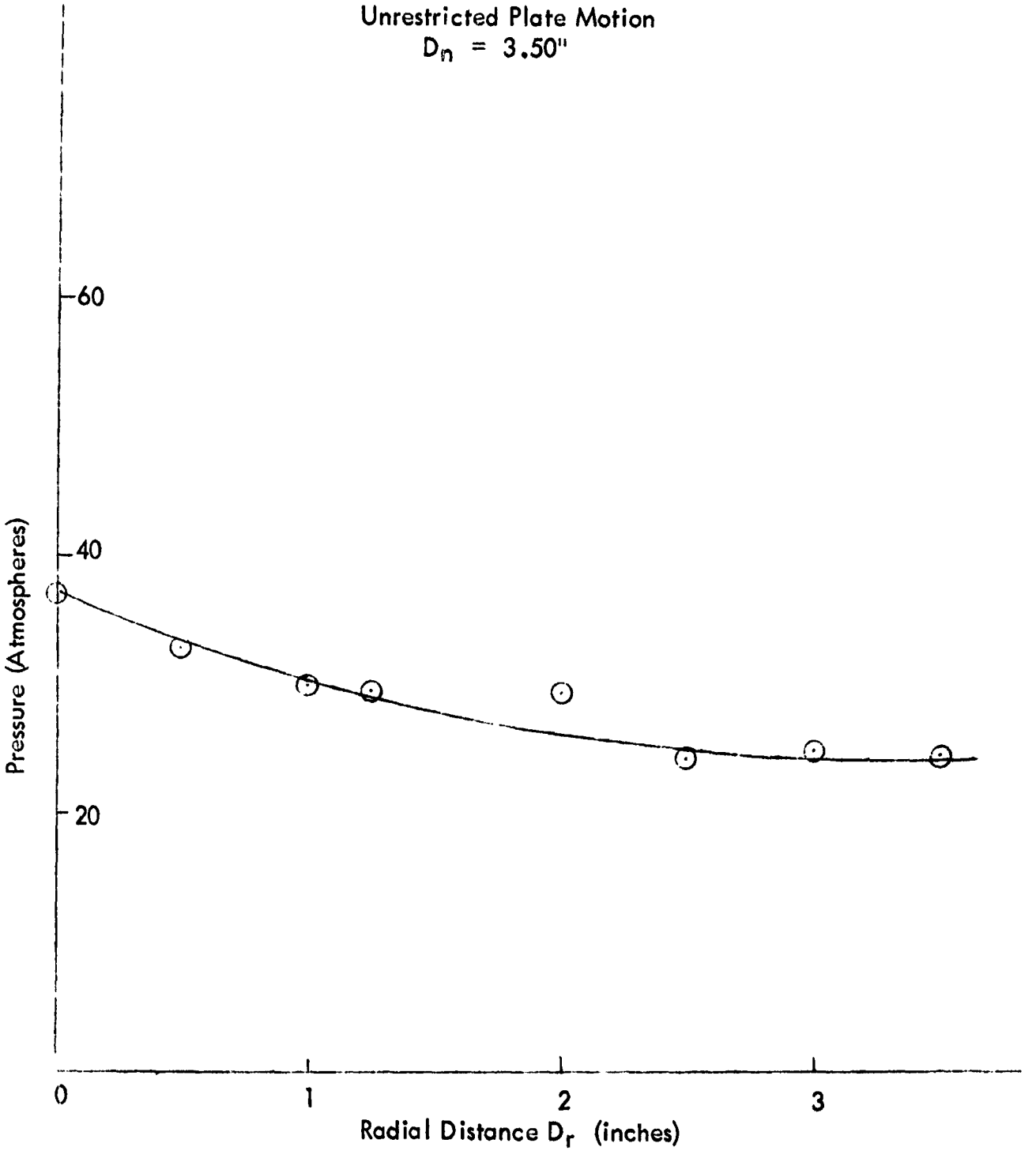

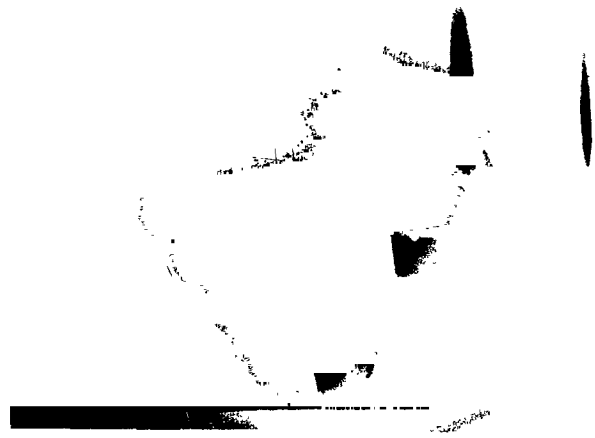

Fig. 10: Photograph of the Coil and Driver Plate Showing Cavitation at 158 μsec after Initiation of the Capacitor Bank Discharge

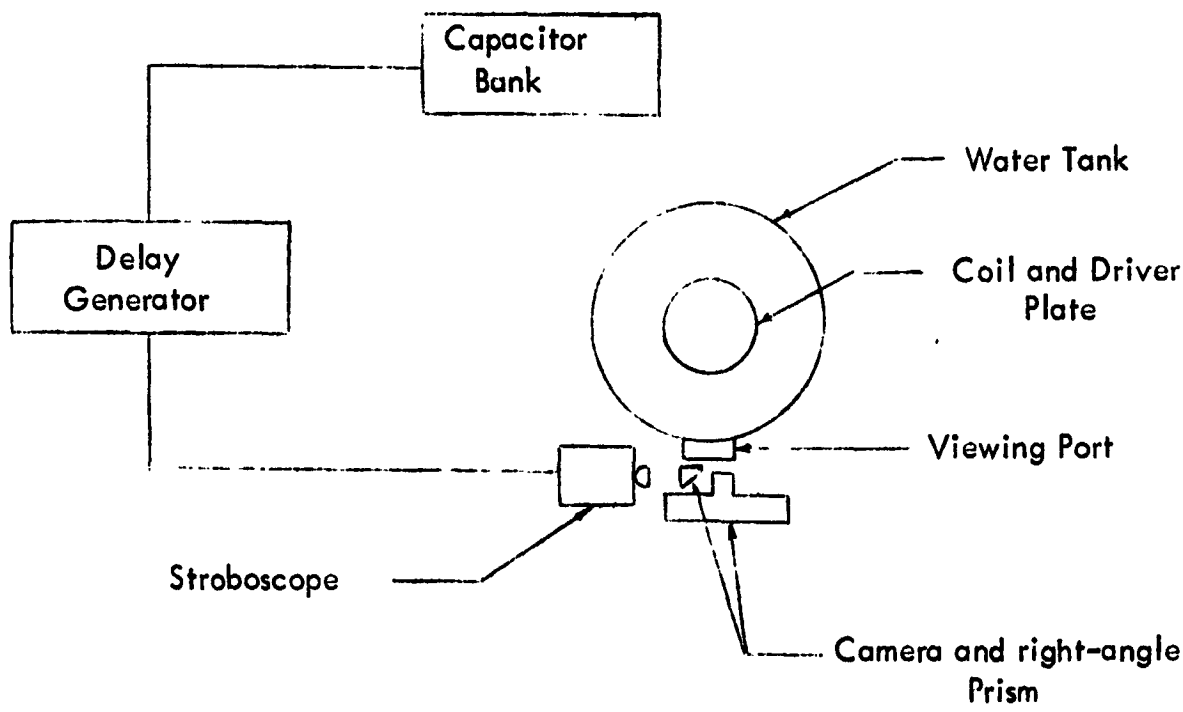

Fig. 11: SCHEMATIC OF EXPERIMENTAL SETUP FOR PHOTOGRAPHIC MEASUREMENTS

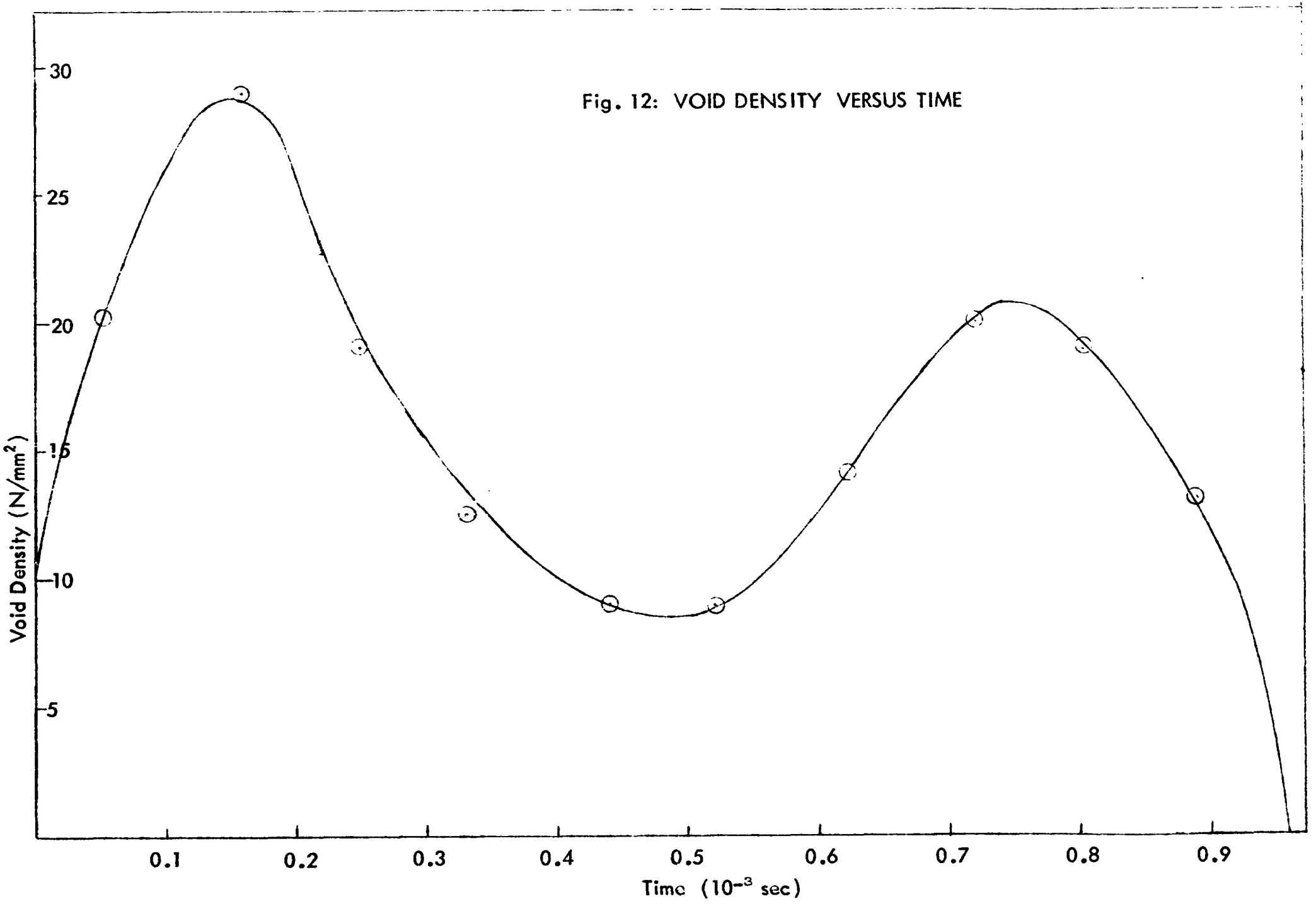

Fig. 12: VOID DENSITY VERSUS TIME

Fig. 13: PRESSURE MEASUREMENTS WITH DRIVER PLATE

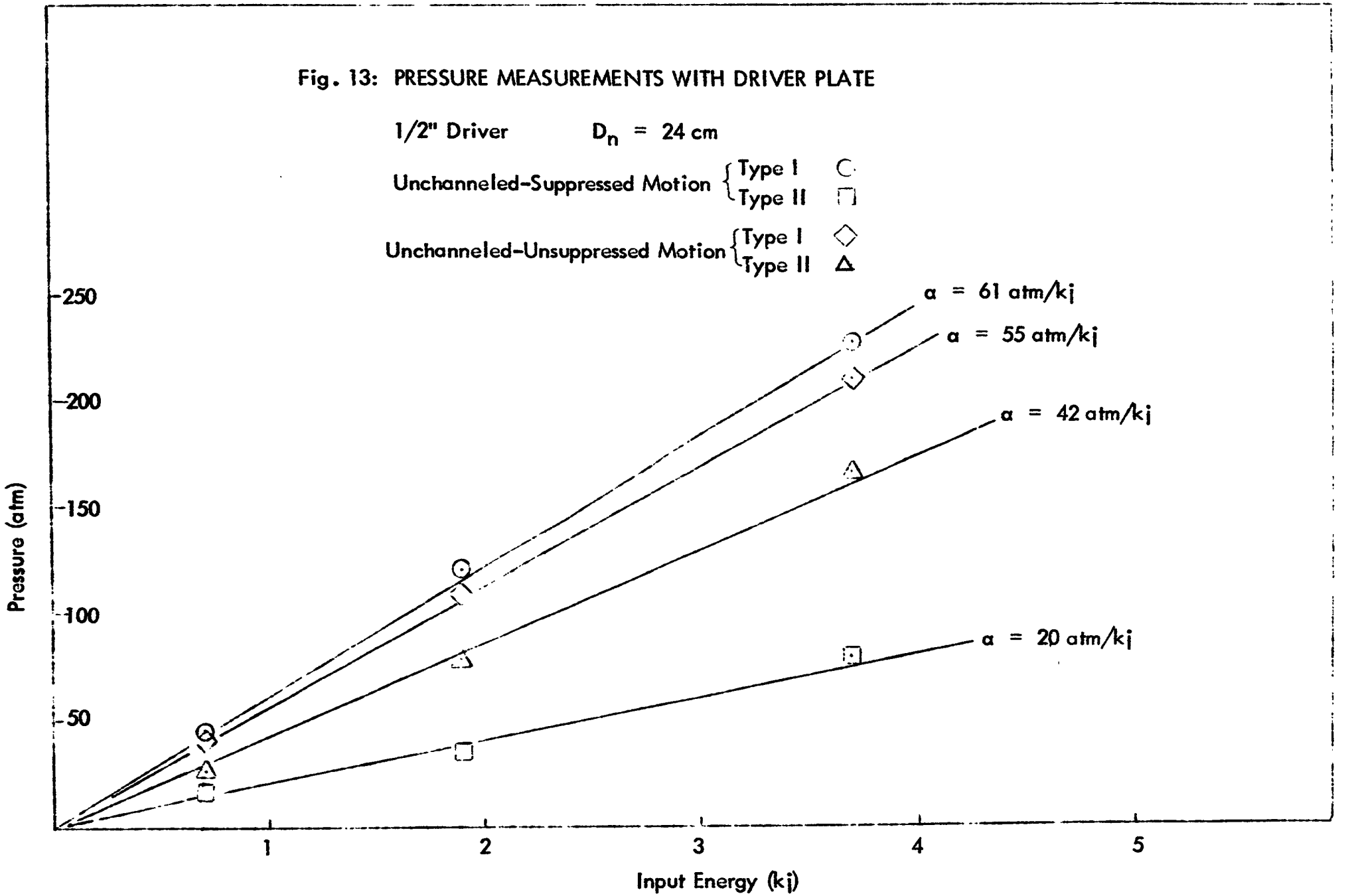

Fig. 14: ATTENUATION OF TYPE I WAVE

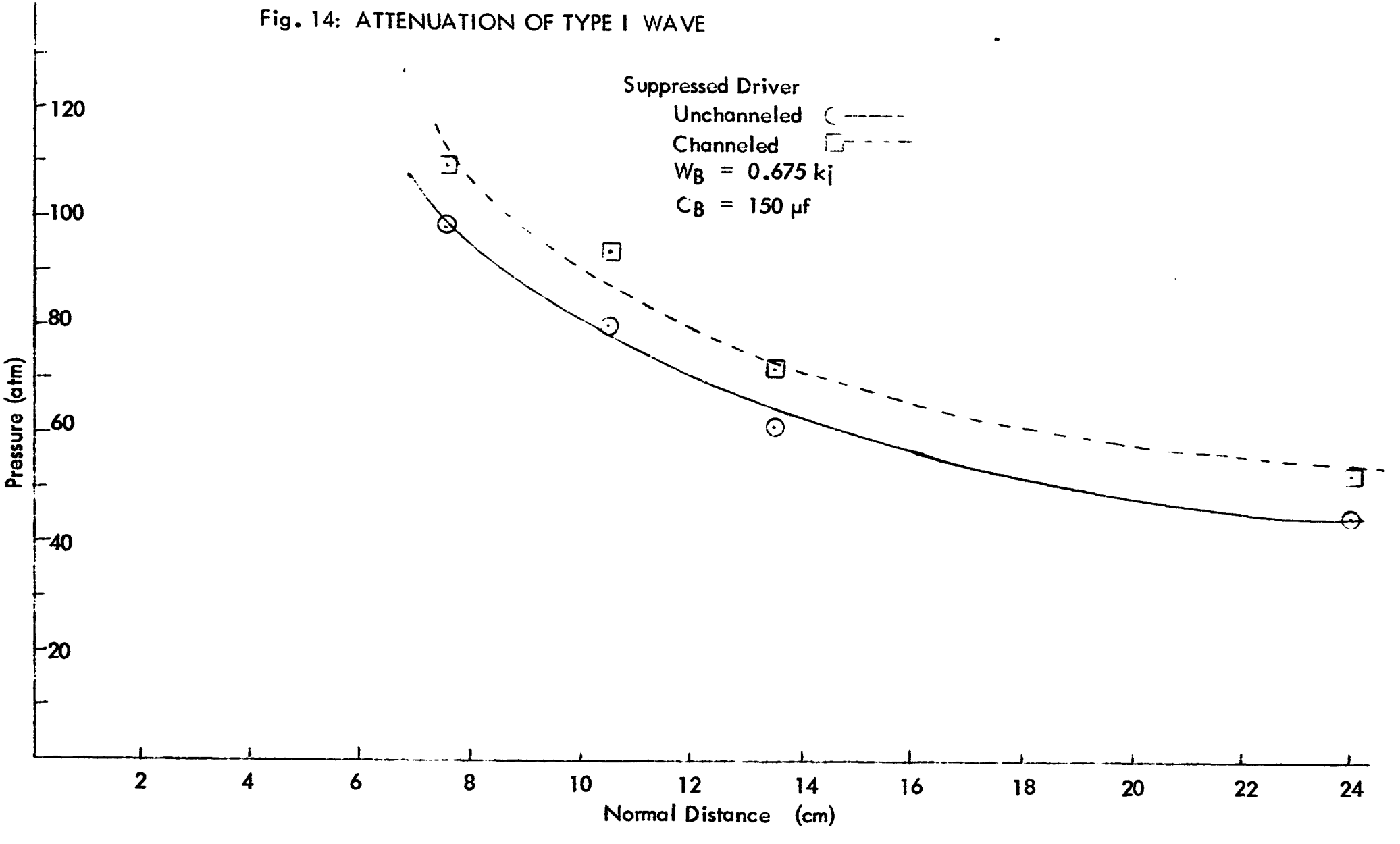

Fig. 15: PRESSURE VERSUS DRIVER PLATE THICKNESS

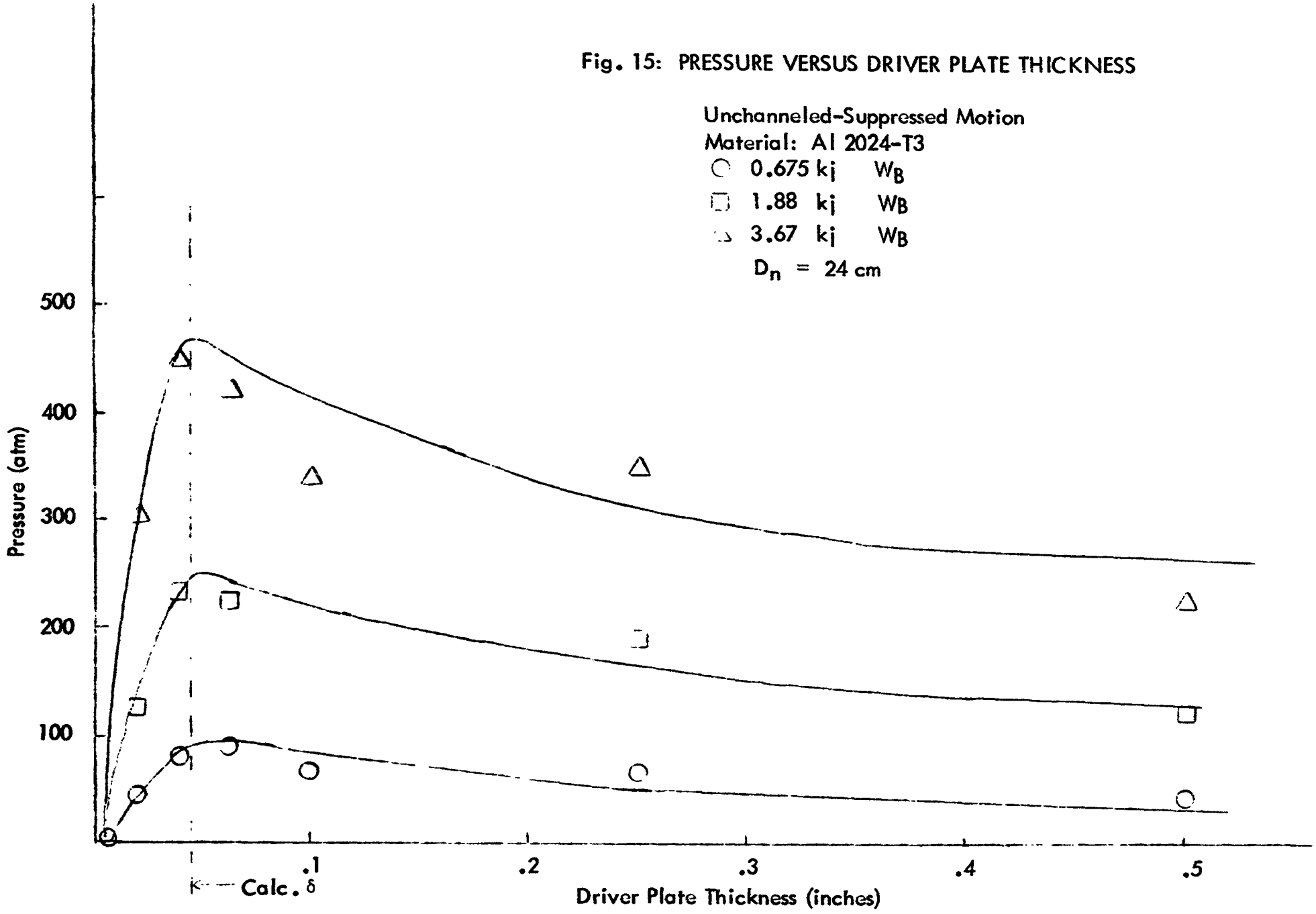

Fig. 16: PRESSURE VERSUS DRIVER PLATE THICKNESS

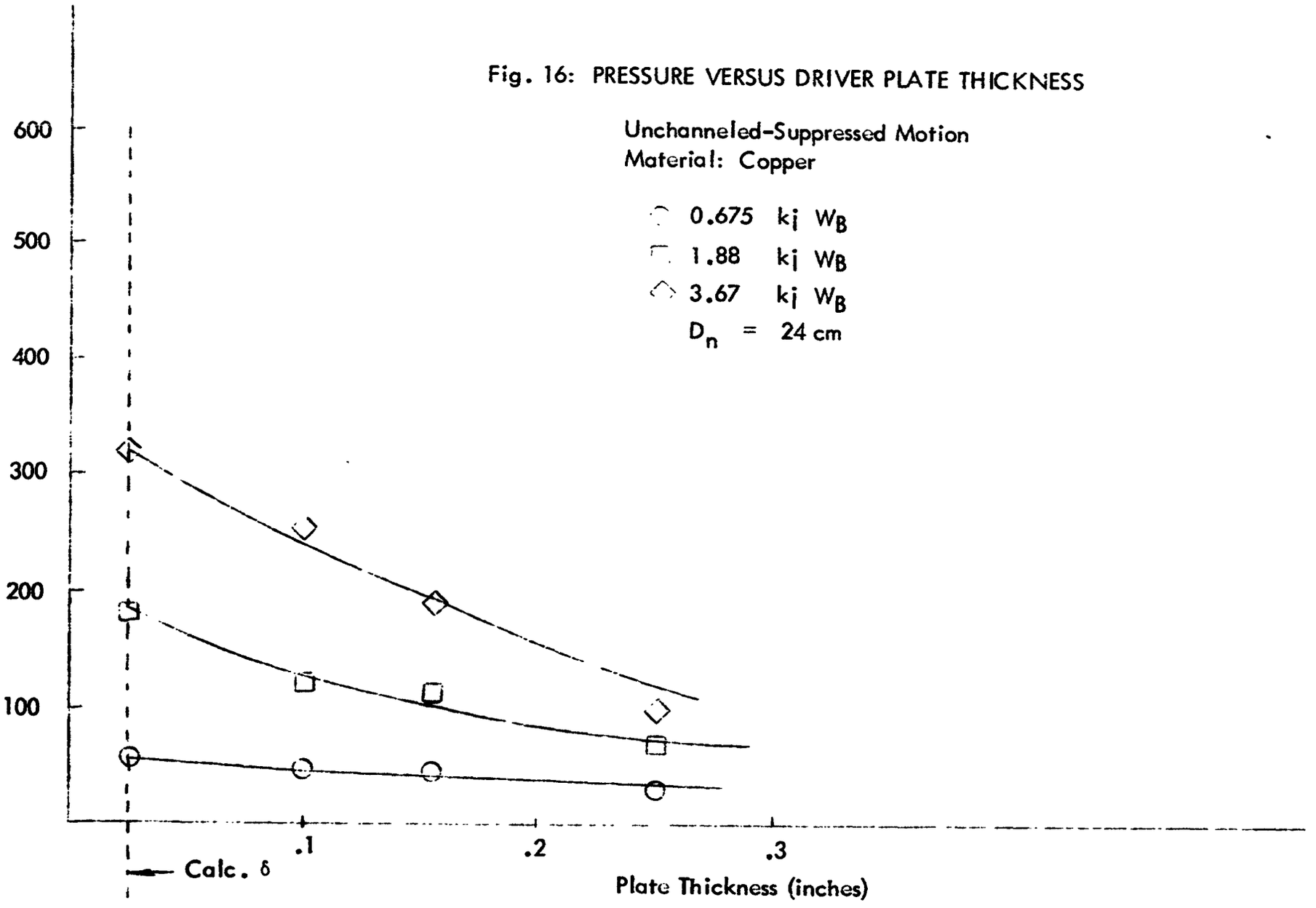

Fig. 17: LINEAR DEFORMATION AL2024-T3 VERSUS DISCHARGE ENERGY

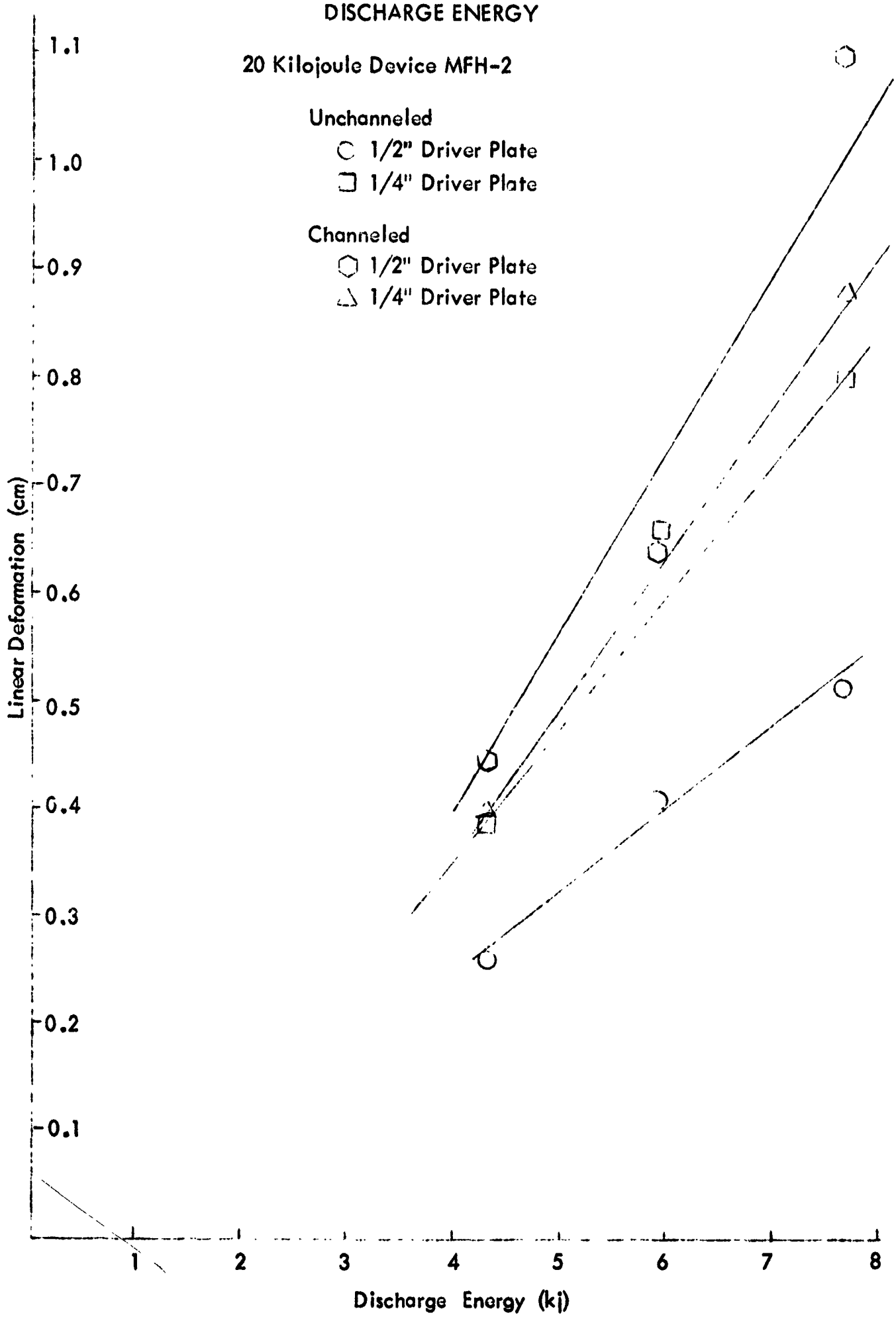

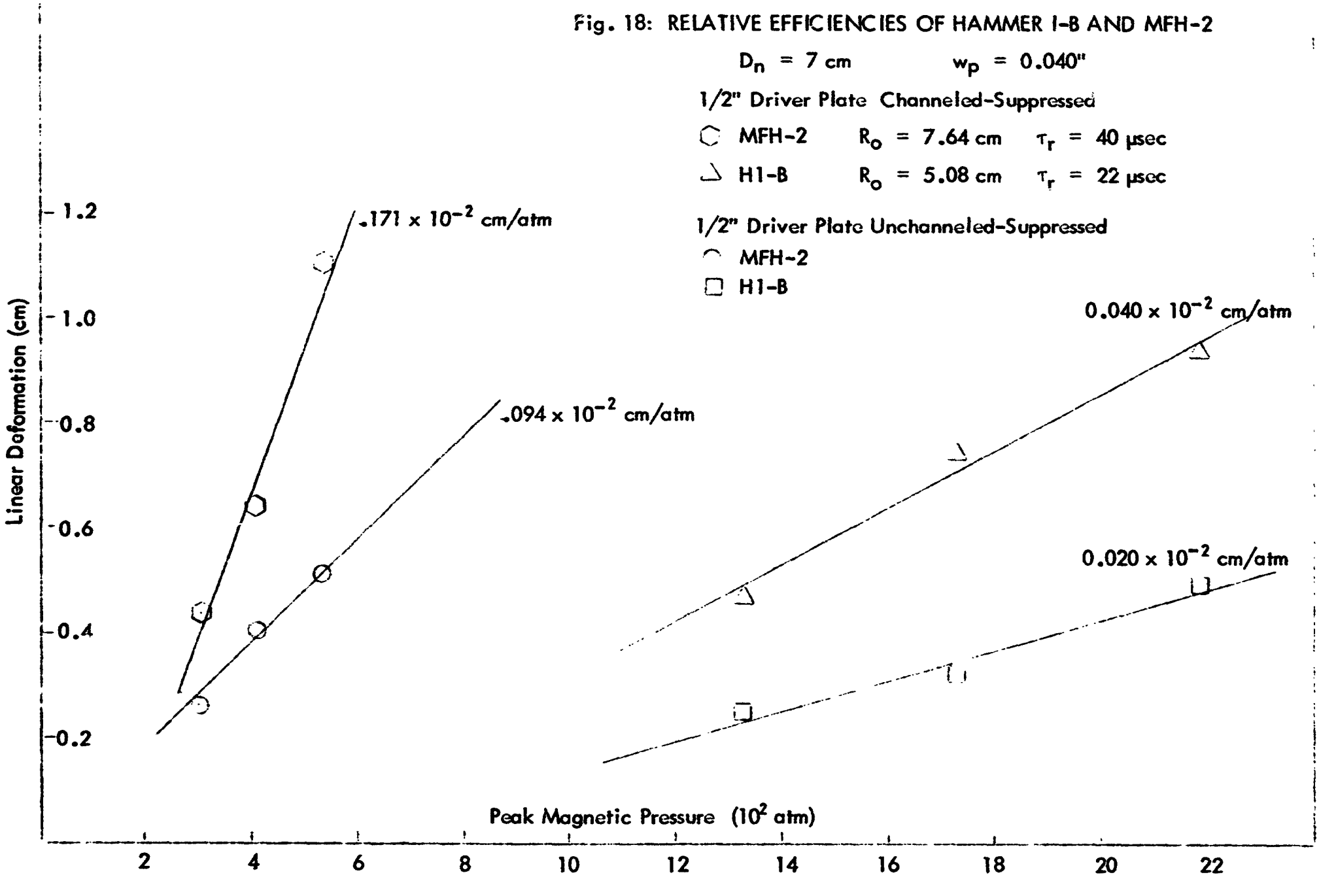
Fig. 18: RELATIVE EFFICIENCIES OF HAMMER I-B AND MFH-2
D_n = 7 cm
w_p = 0.040"
1/2" Driver Plate Channeled-Suppressed
MFH-2 R_o = 7.64 cm τ_r = 40 μsec
H1-B R_o = 5.08 cm τ_r = 22 μsec
1/2" Driver Plate Unchanneled-Suppressed
MFH-2
H1-B
.171 x 10^{-2} cm/atm
.094 x 10^{-2} cm/atm
0.040 x 10^{-2} cm/atm
0.020 x 10^{-2} cm/atm
Linear Deformation (cm)
1.2
1.0
0.8
0.6
0.4
0.2
Peak Magnetic Pressure (10^2 atm)
2
4
6
8
10
12
14
16
18
20
22

Fig. 12: LINEAR DEFORMATION AL2024-T3 VERSUS MAGNETIC FIELD DURATION (τ_r)

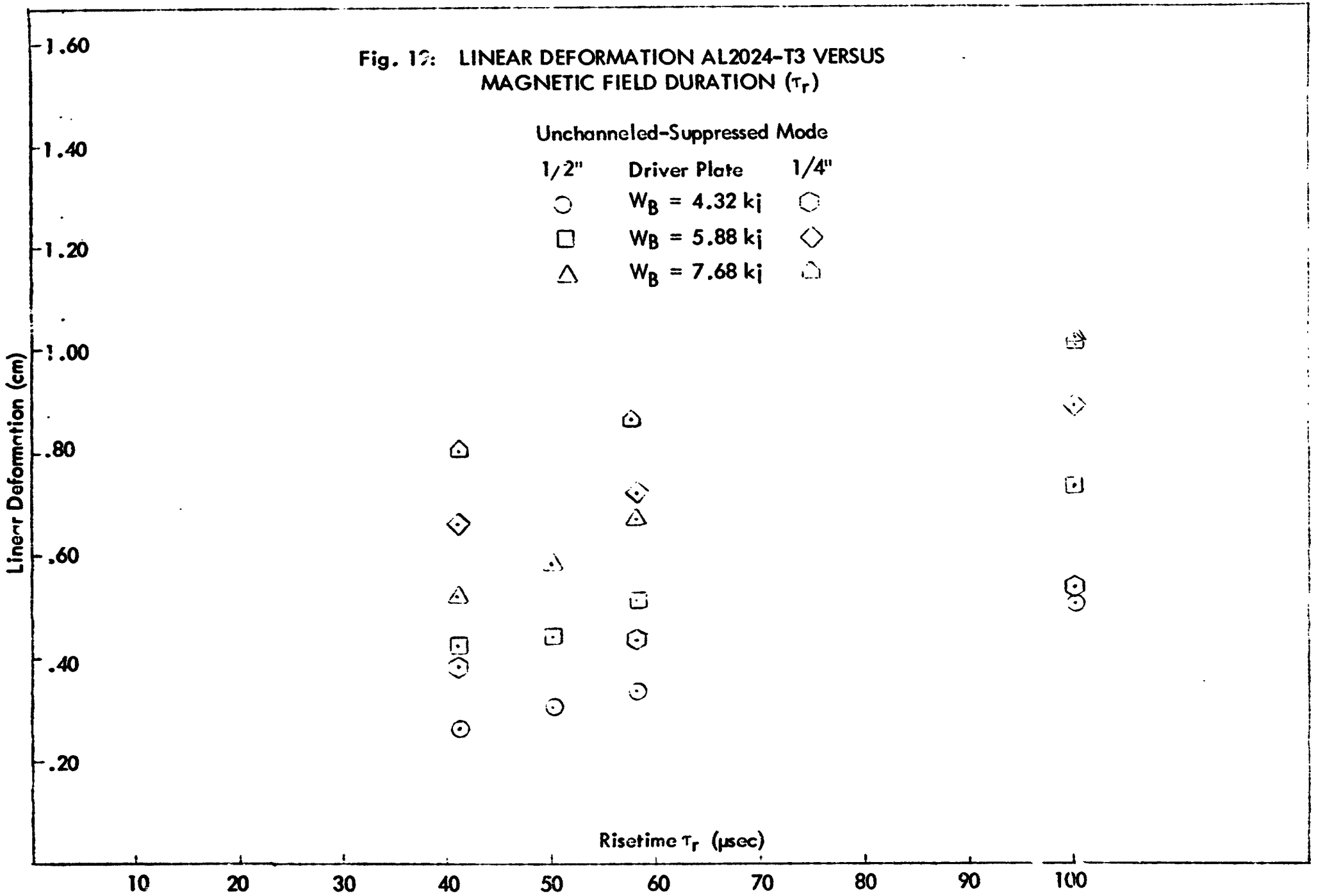

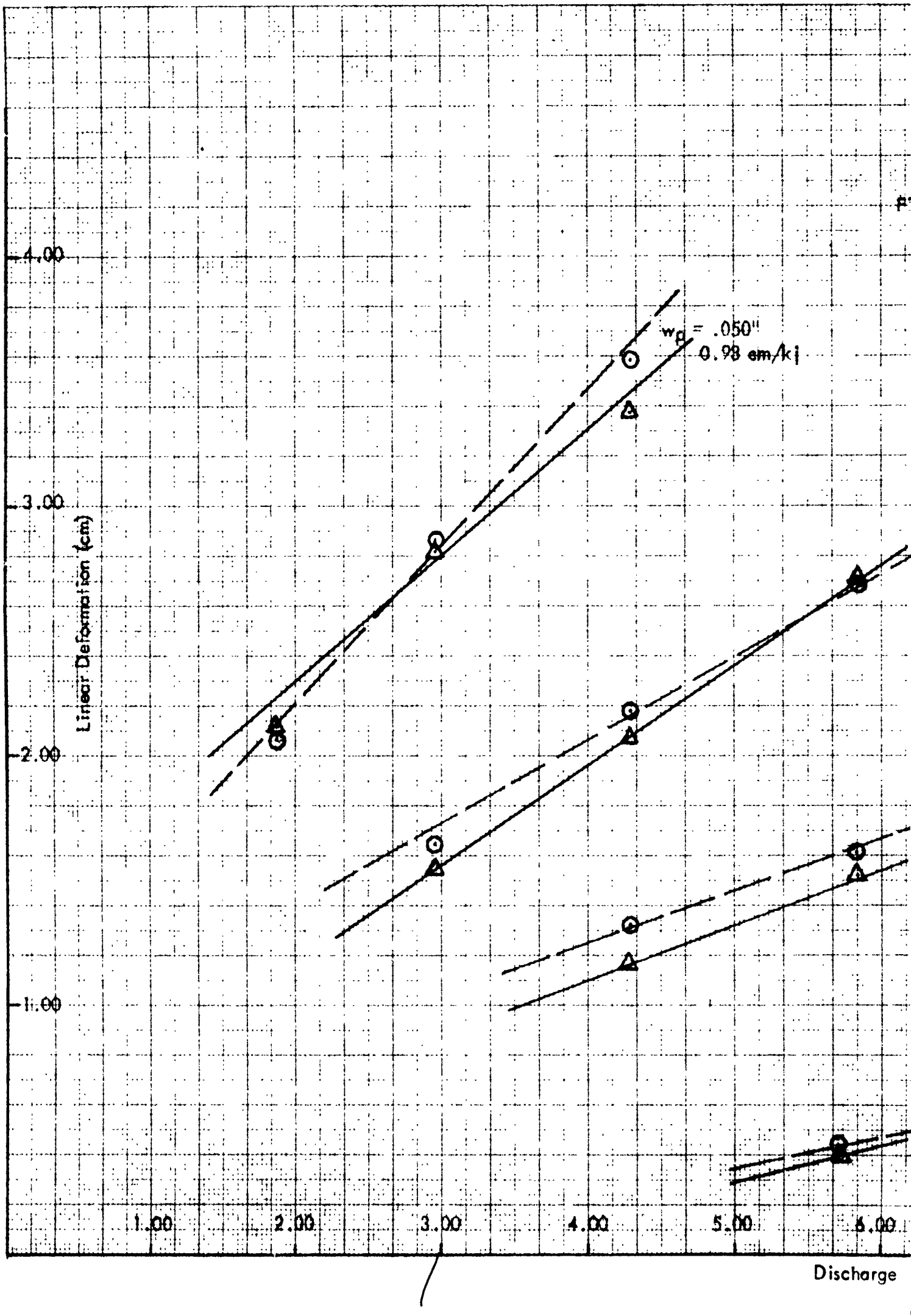
4.00
3.00
2.00
1.00
Linear Deformation (cm)
w_d = .050"
0.98 cm/kj
1.00
2.00
3.00
4.00
5.00
6.00
Discharge

Fig. 20: LINEAR DEFORMATION IN AIR AL 6061-T6
vs
DISCHARGE ENERGY

MFH-2 Coil and Coaxial Line Assembly
w_p = Work piece thickness
△ = Deformation with Oscillatory Circuit
○ = Deformation with Crowbar Circuit

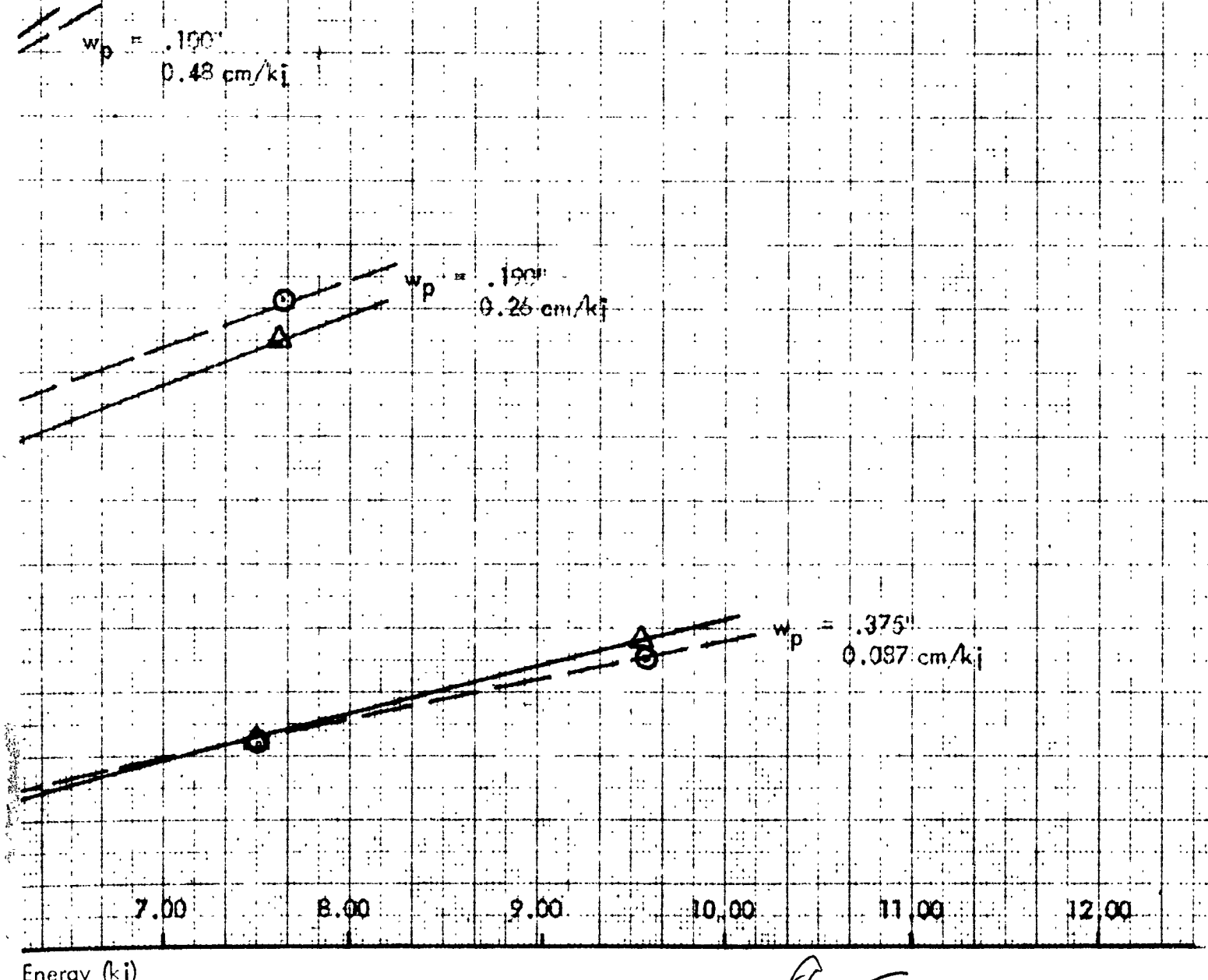

Fig. 21: CROWBARRING CIRCUITRY FOR 20 KILOJOULE DEVICE

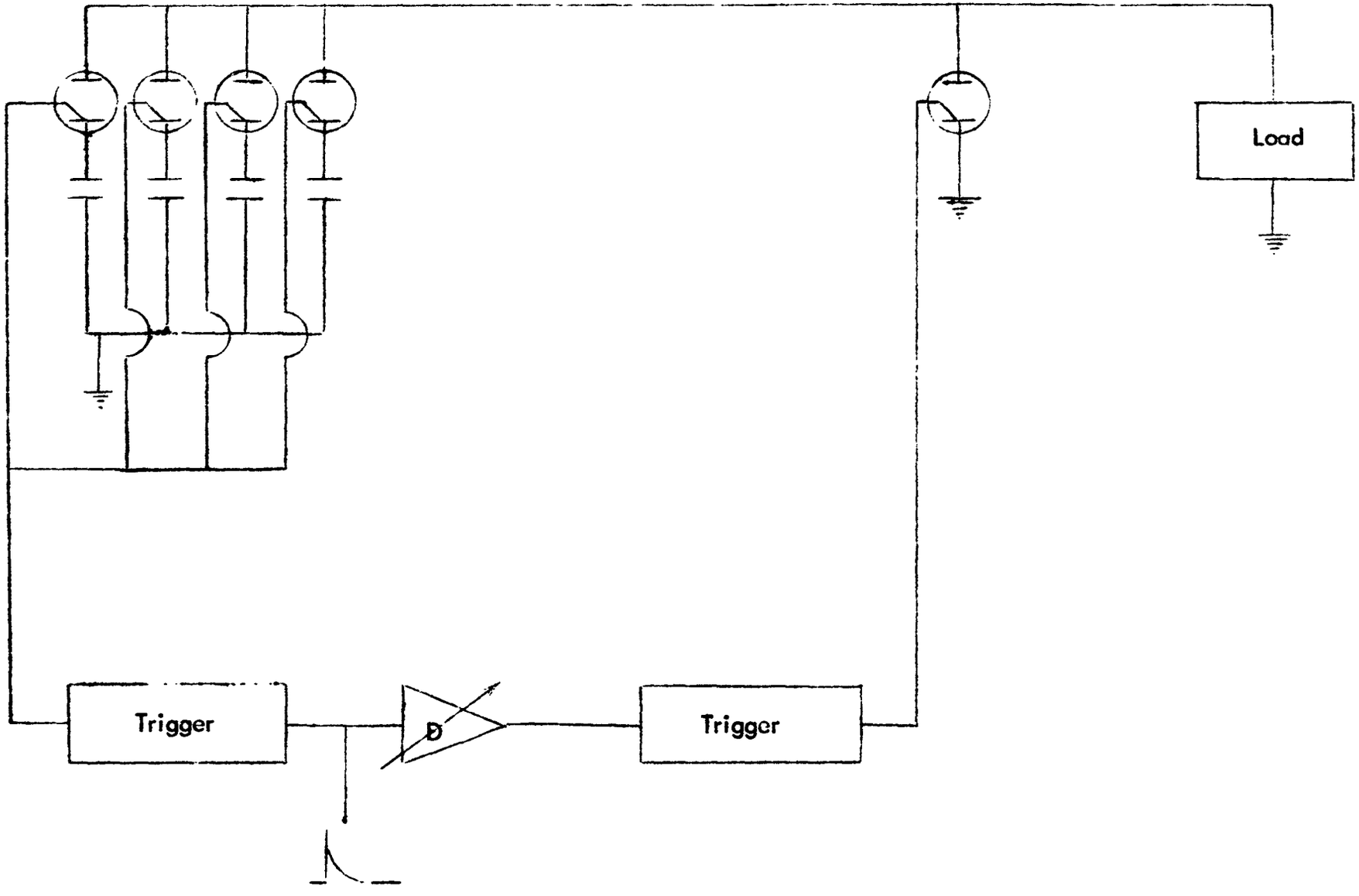

Fig. 22: LINEAR DEFORMATION AL2024-T3 VERSUS DISCHARGE ENERGY

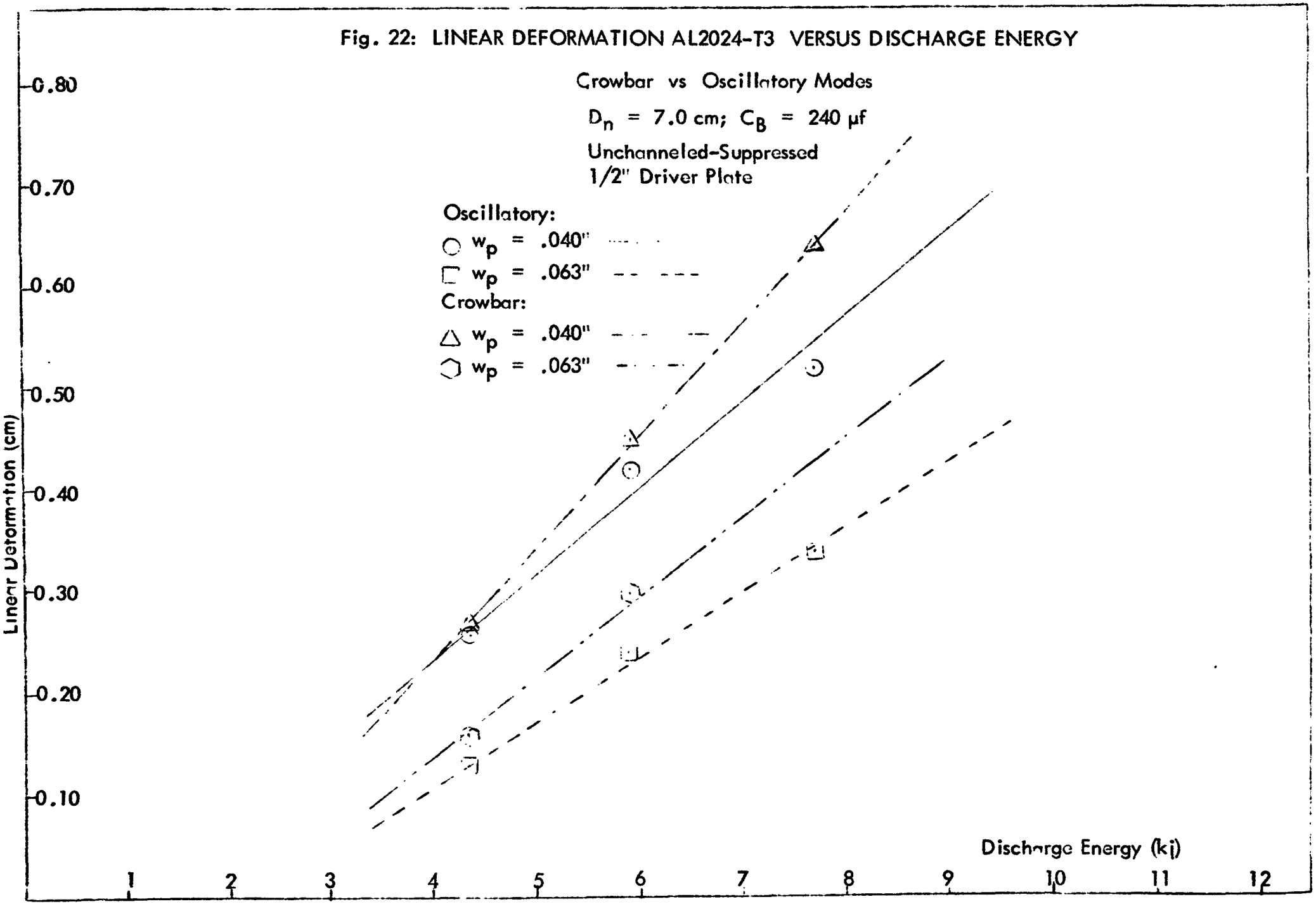

Fig. 23: SCHEMATIC ILLUSTRATION OF EQUIPMENT FOR ATTENUATION MEASUREMENT

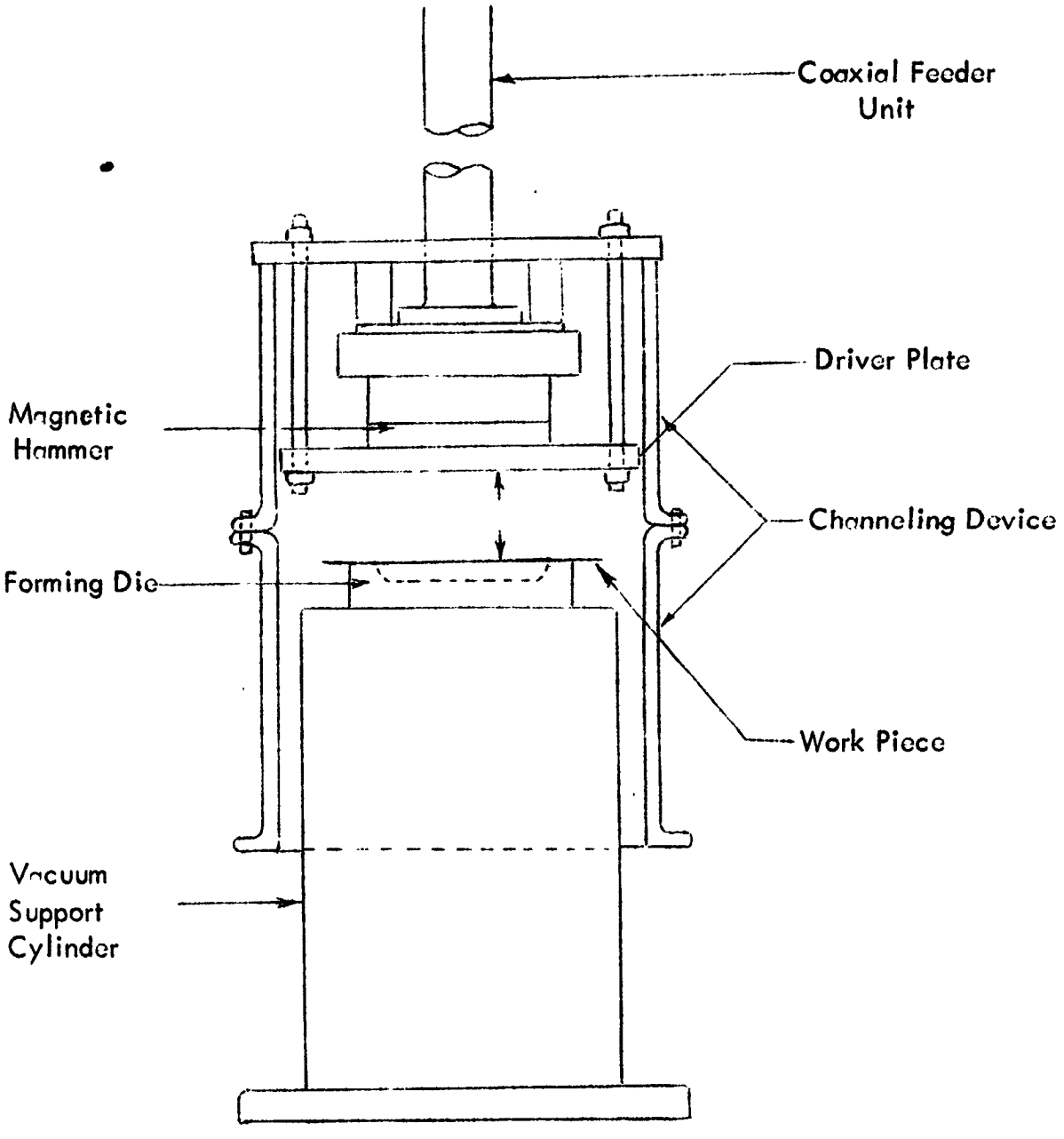

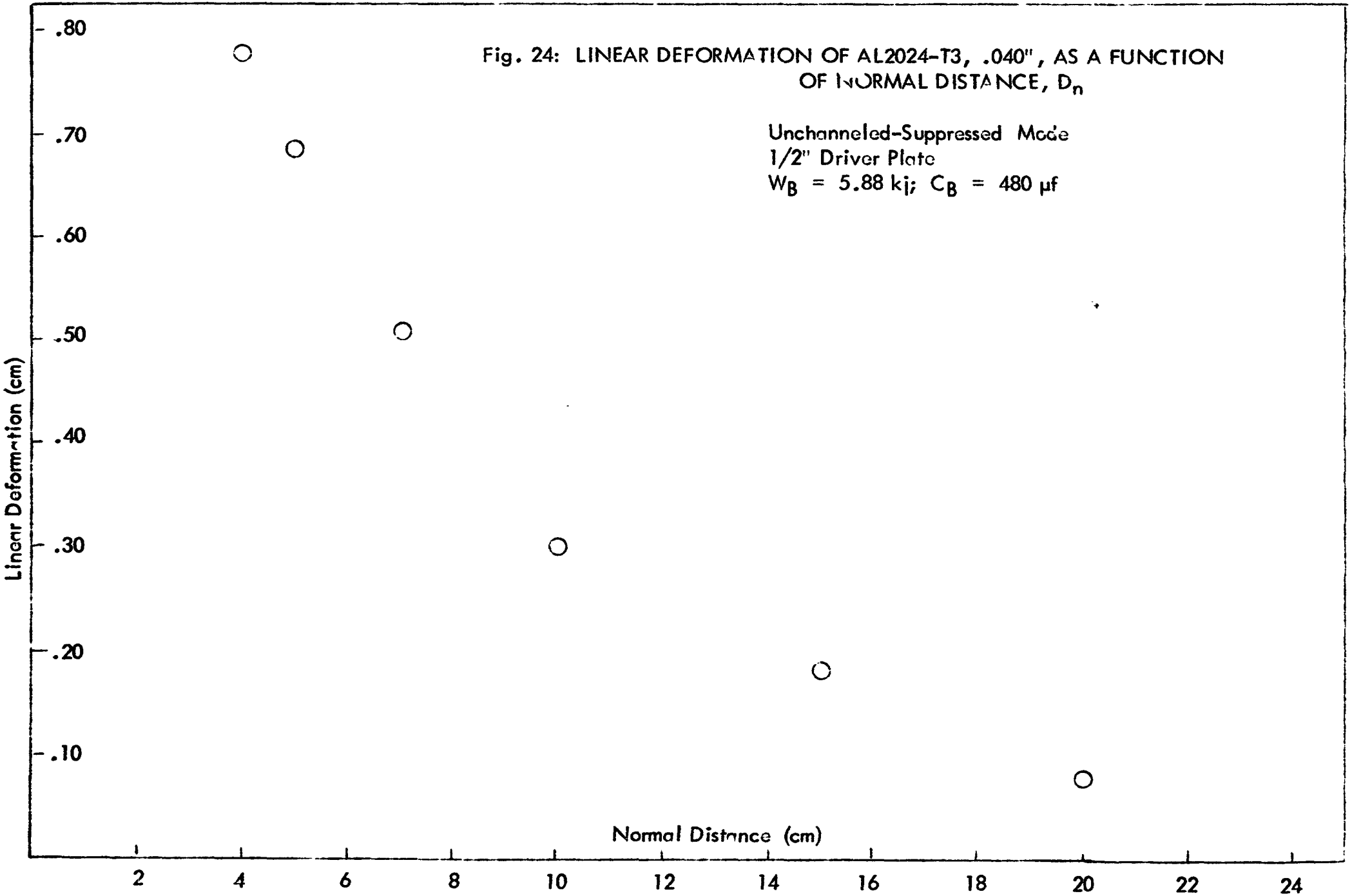
Fig. 24: LINEAR DEFORMATION OF AL2024-T3, .040", AS A FUNCTION OF NORMAL DISTANCE, D_n
Unchanneled-Suppressed Mode
1/2" Driver Plate
W_B = 5.88 kj; C_B = 480 μf
Linear Deformation (cm)
.80
.70
.60
.50
.40
.30
.20
.10
Normal Distance (cm)
2
4
6
8
10
12
14
16
18
20
22
24

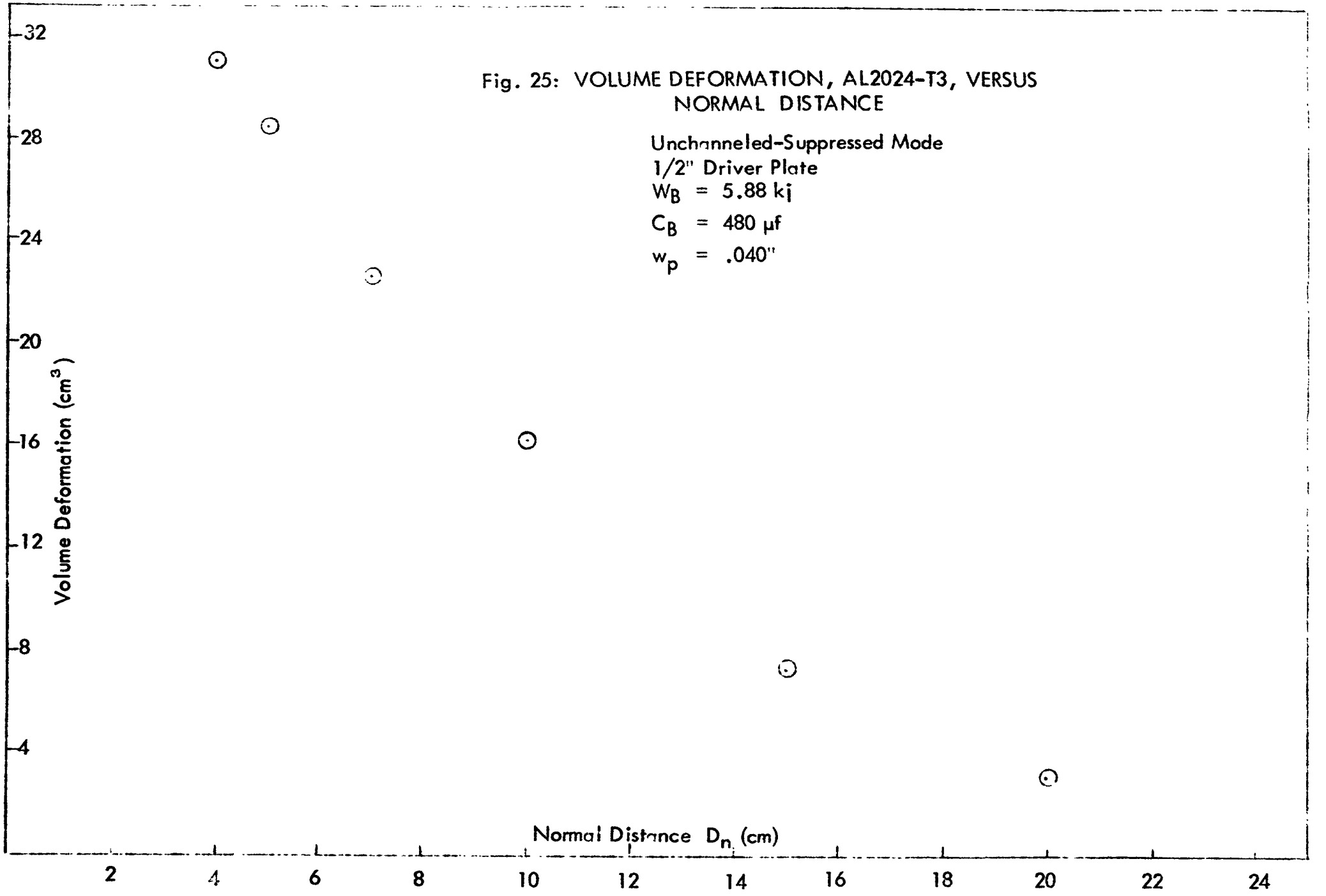

Fig. 25: VOLUME DEFORMATION, AL2024-T3, VERSUS NORMAL DISTANCE

Unchanneled-Suppressed Mode
1/2" Driver Plate
W_B = 5.88 kj
C_B = 480 μf
w_p = .040"

Fig. 26: LINEAR DEFORMATION AL2024-T3 VERSUS NORMAL DISTANCE, D_n

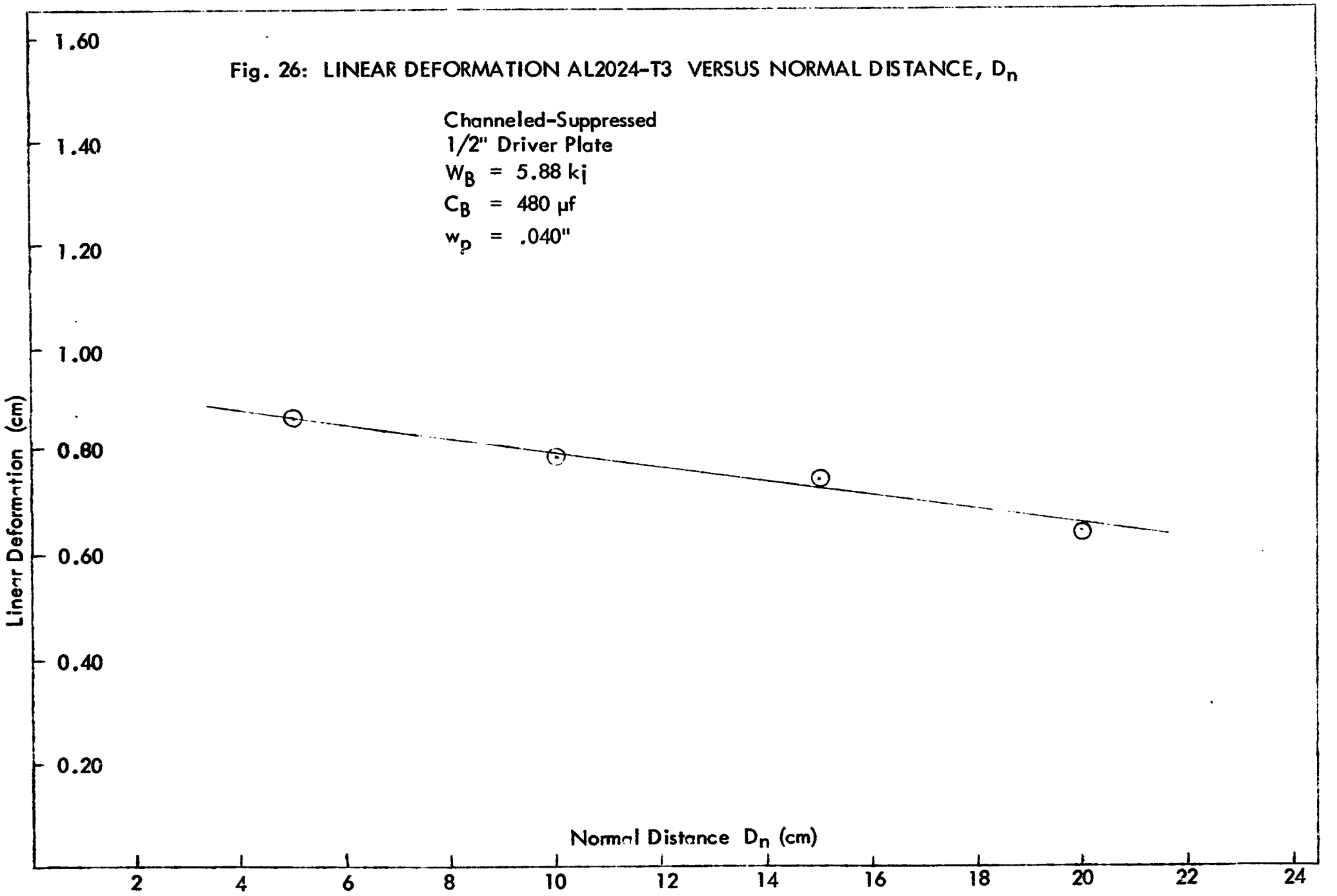

Fig. 27: VOLUME DEFORMATION AL2024-T3 VERSUS NORMAL DISTANCE, D_n

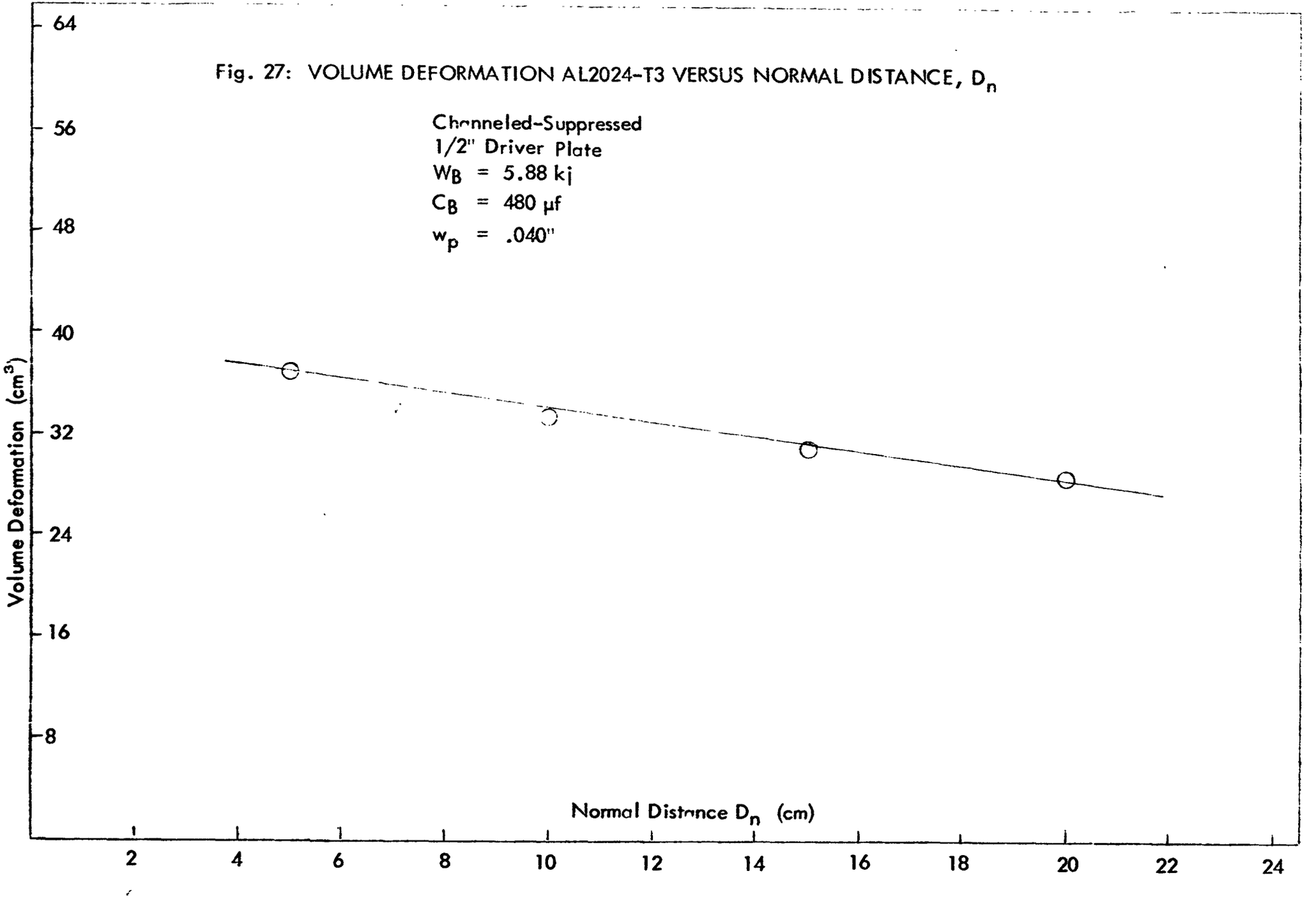

Fig. 28: ATTENUATION OF TYPE I WAVE

1/2" Aluminum Driver - Suppressed w/Concentrator
W_B = 675 joules

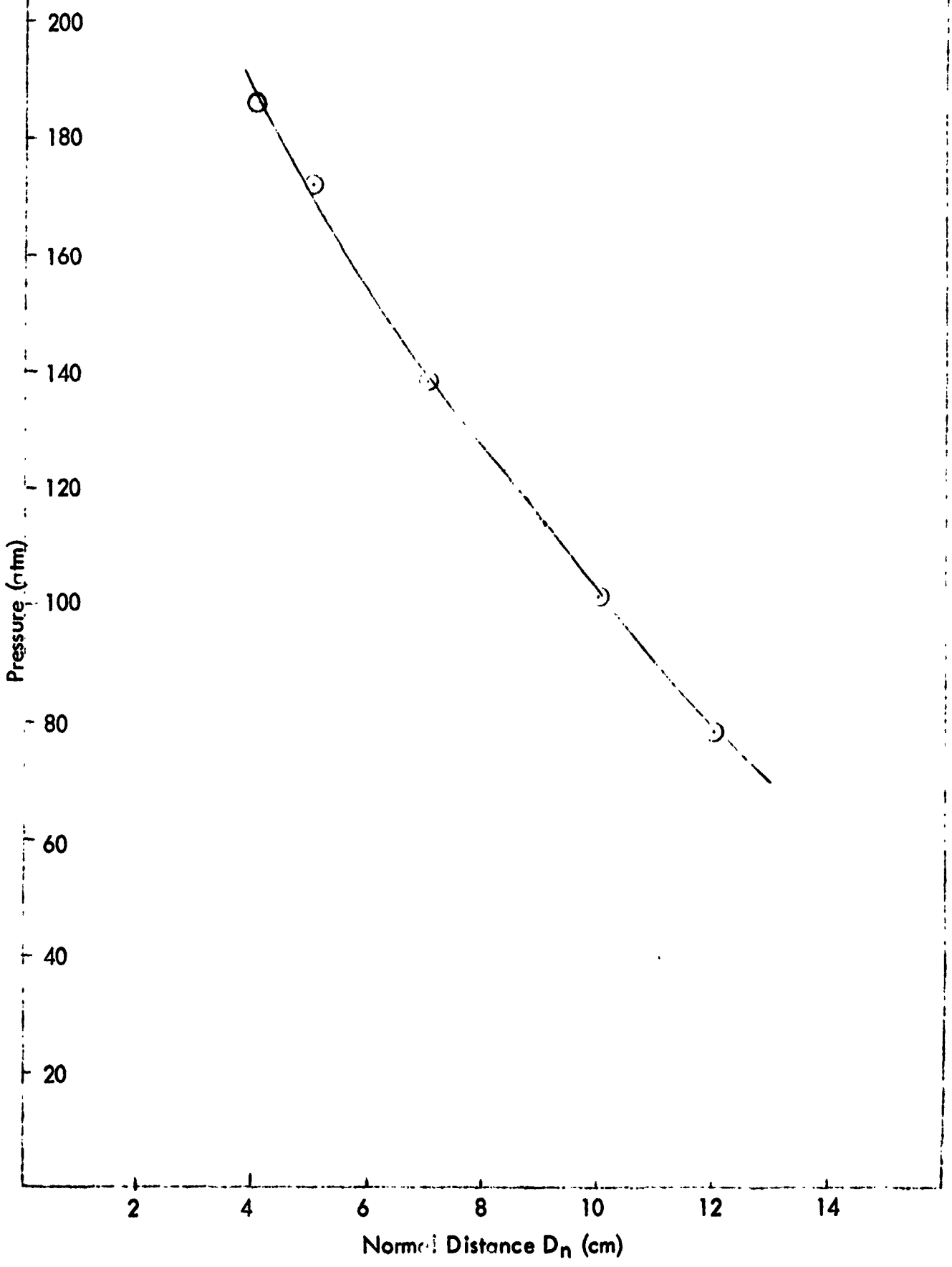

Fig. 29: SCHEMATIC ILLUSTRATION OF CONCENTRATING DEVICE

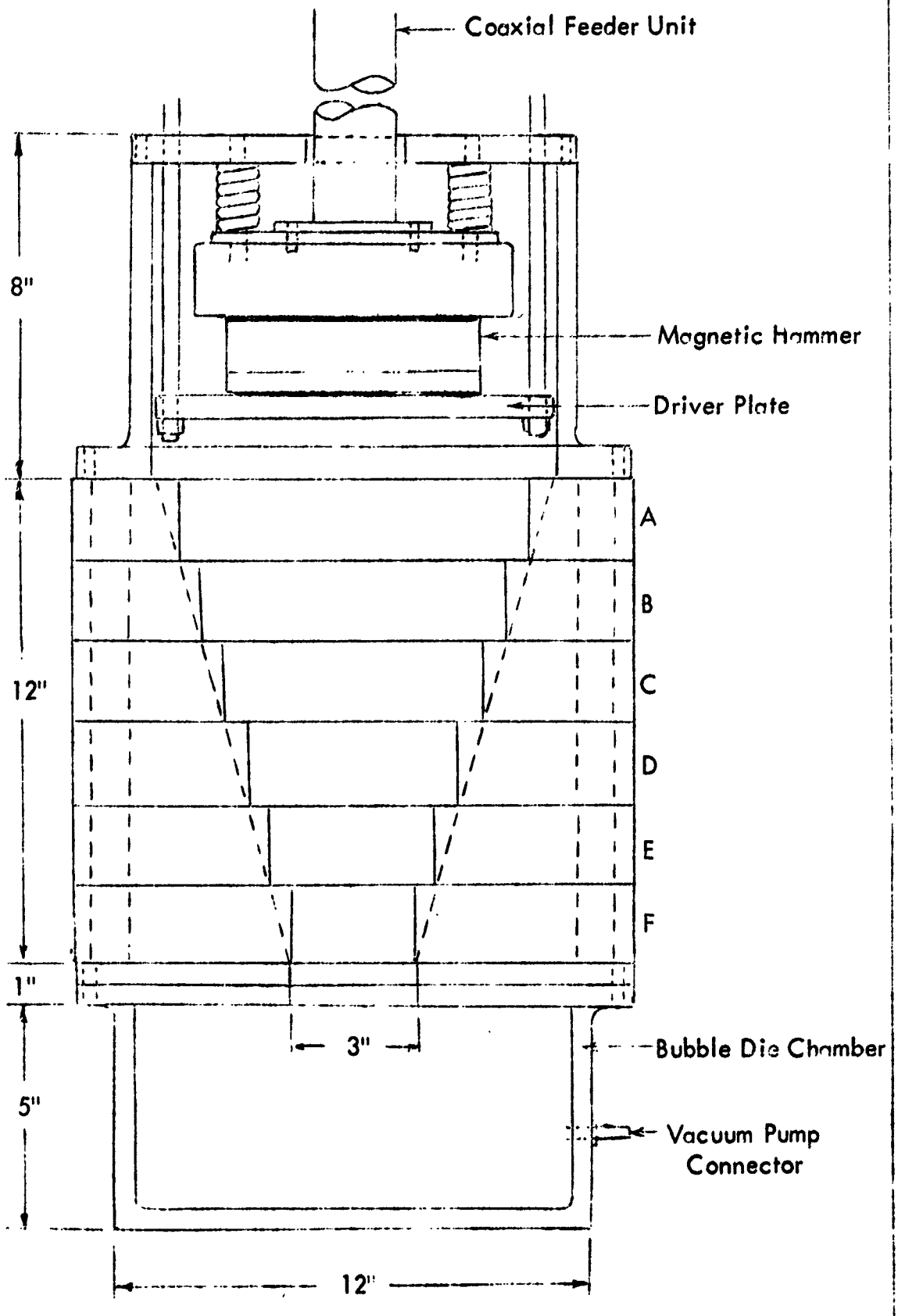

Fig. 30: LINEAR DEFORMATION VERSUS ENERGY

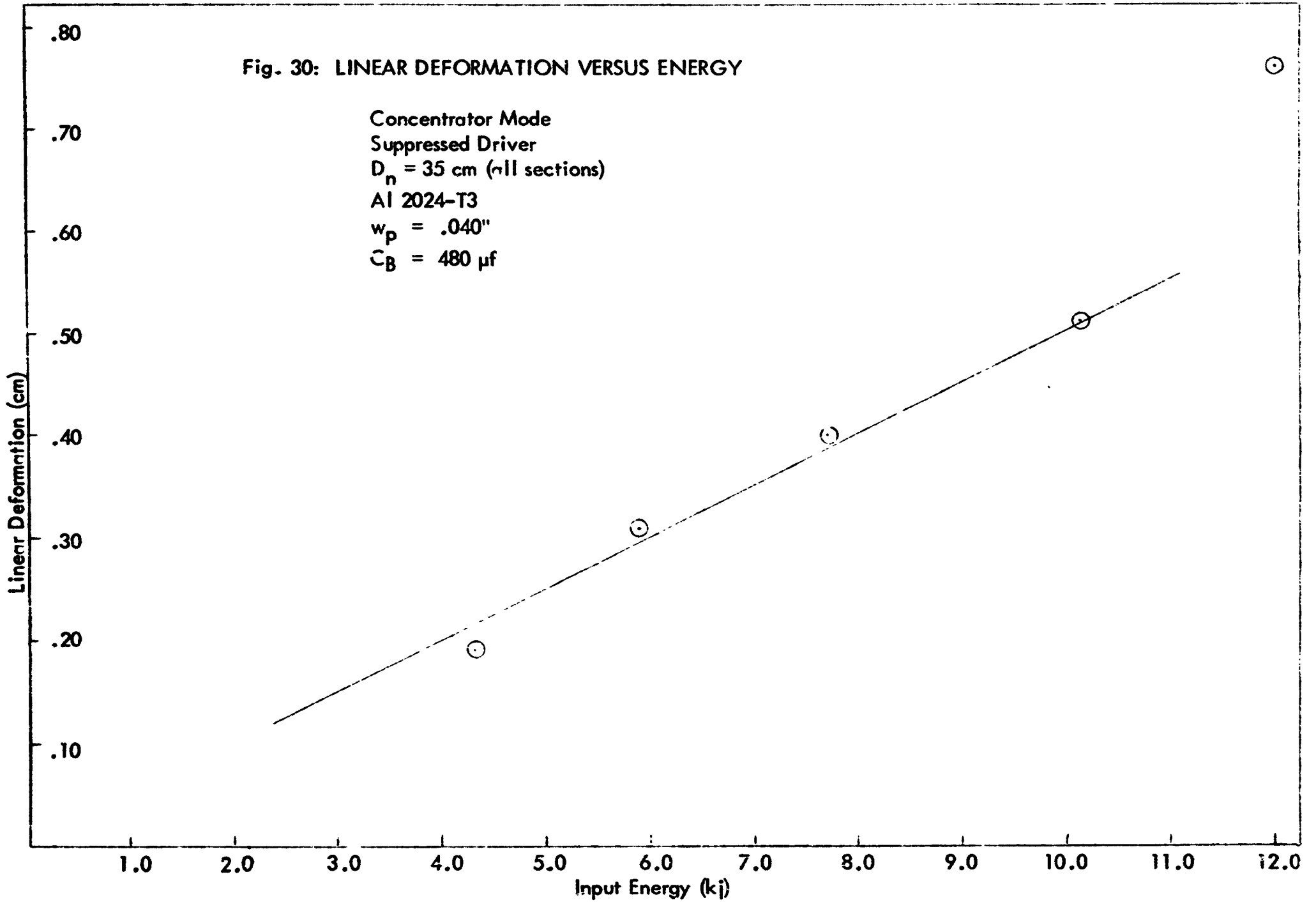

Fig. 31: LINEAR DEFORMATION VERSUS NORMAL DISTANCE

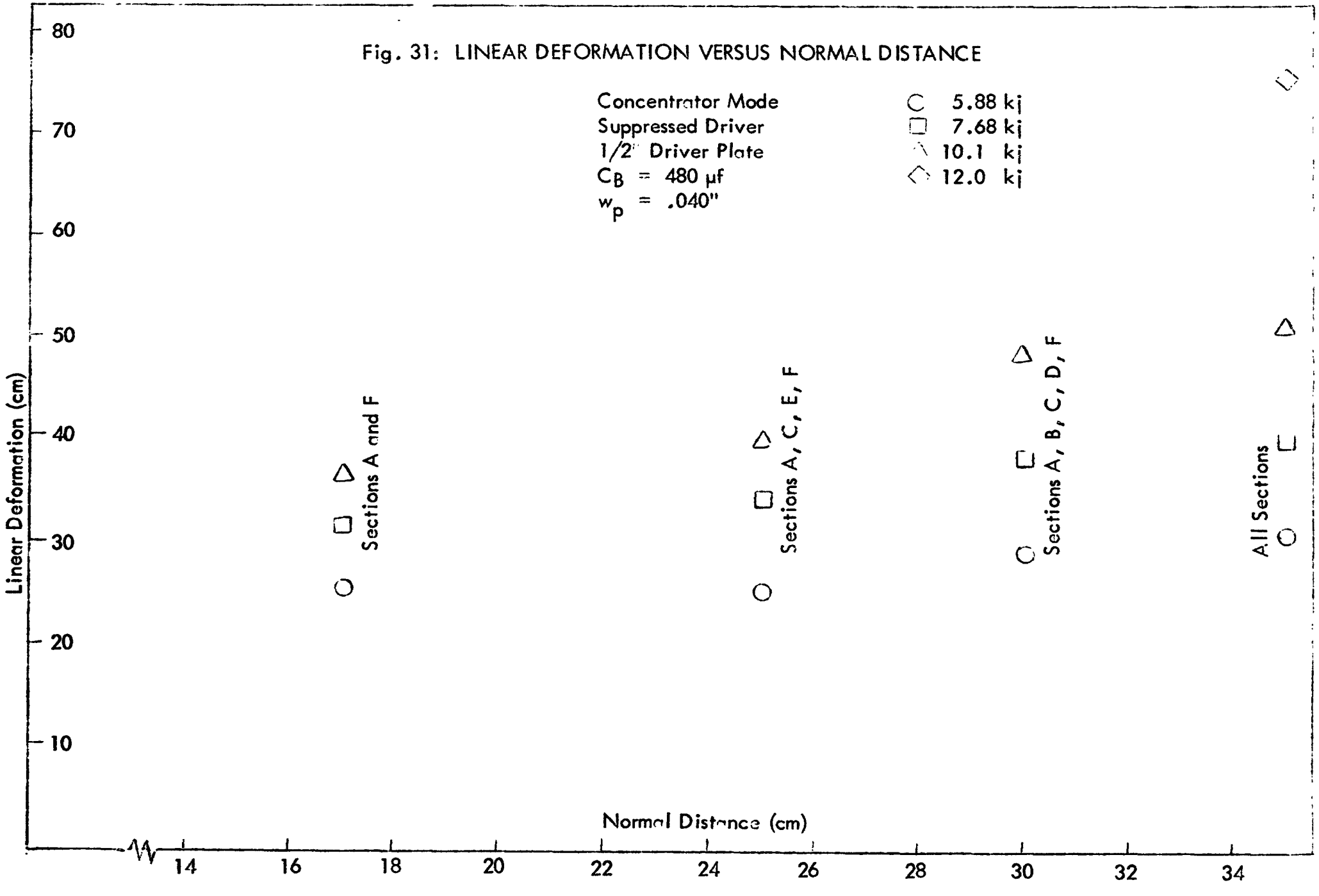

Fig. 32: LINEAR DEFORMATION AL2024-T3 VERSUS DISCHARGE ENERGY

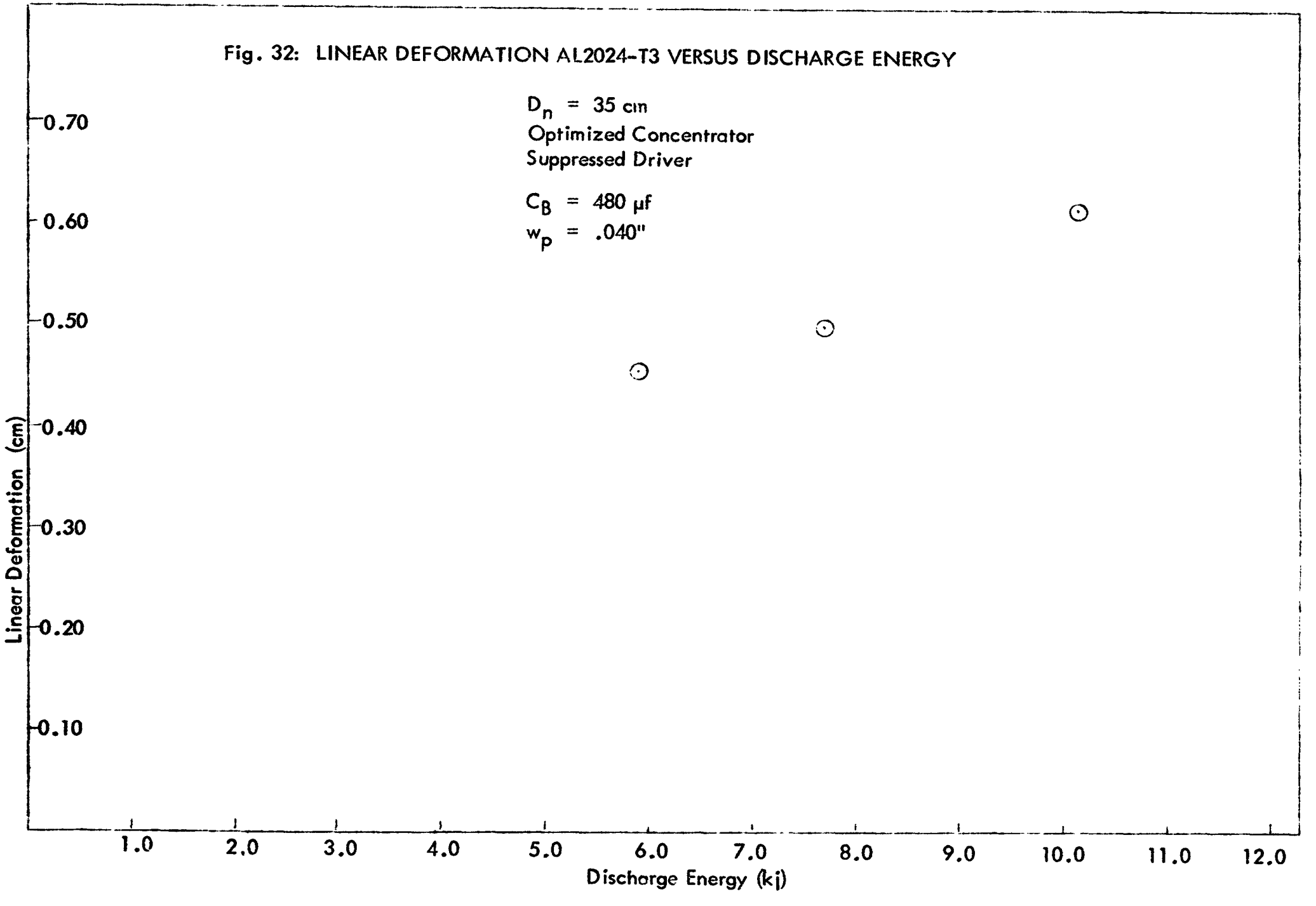

Fig. 33: SCHEMATIC ILLUSTRATION OF CONFINED MODE

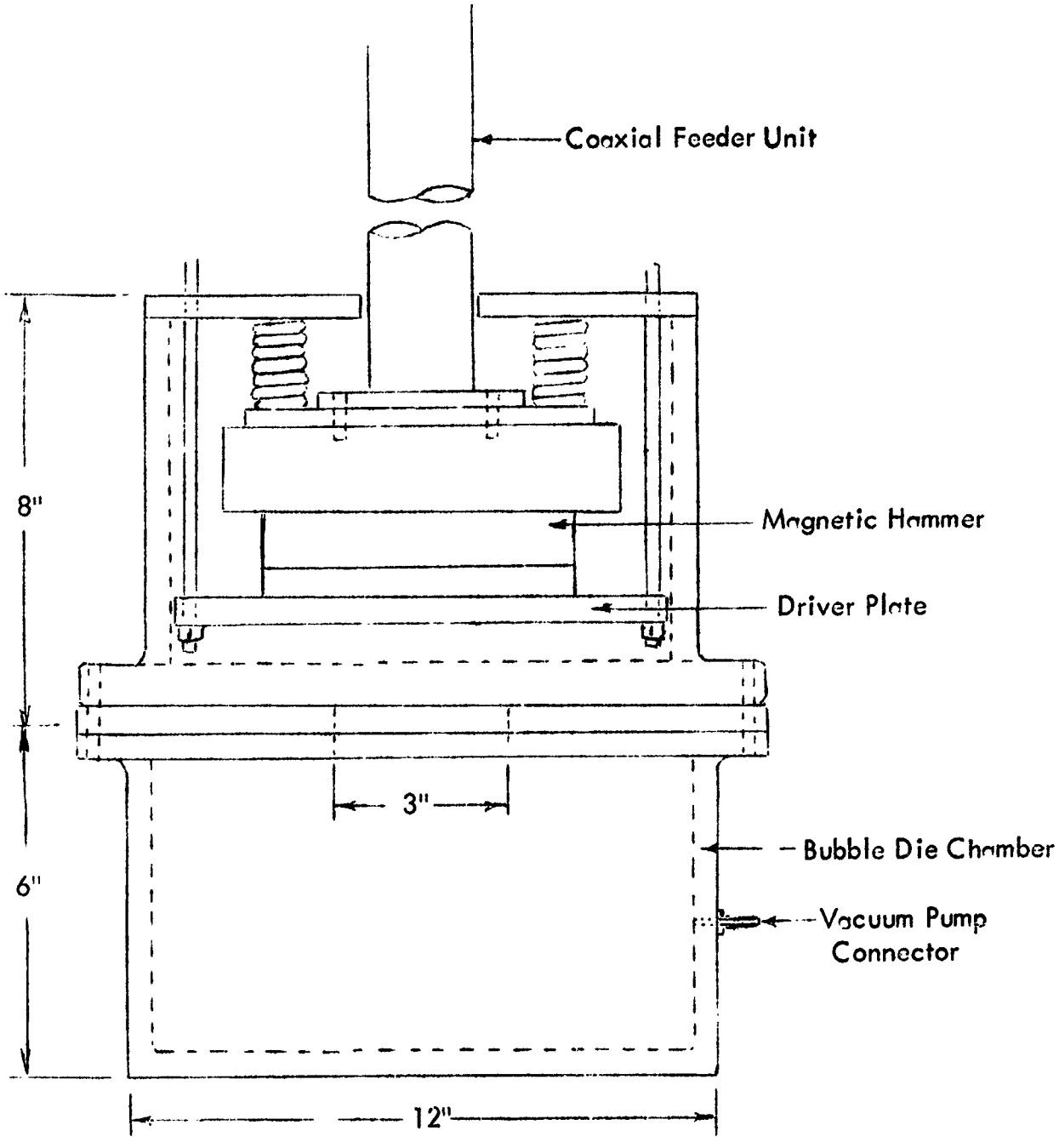

Fig. 34: LINEAR DEFORMATION AL2024-T3 VERSUS DISCHARGE ENERGY

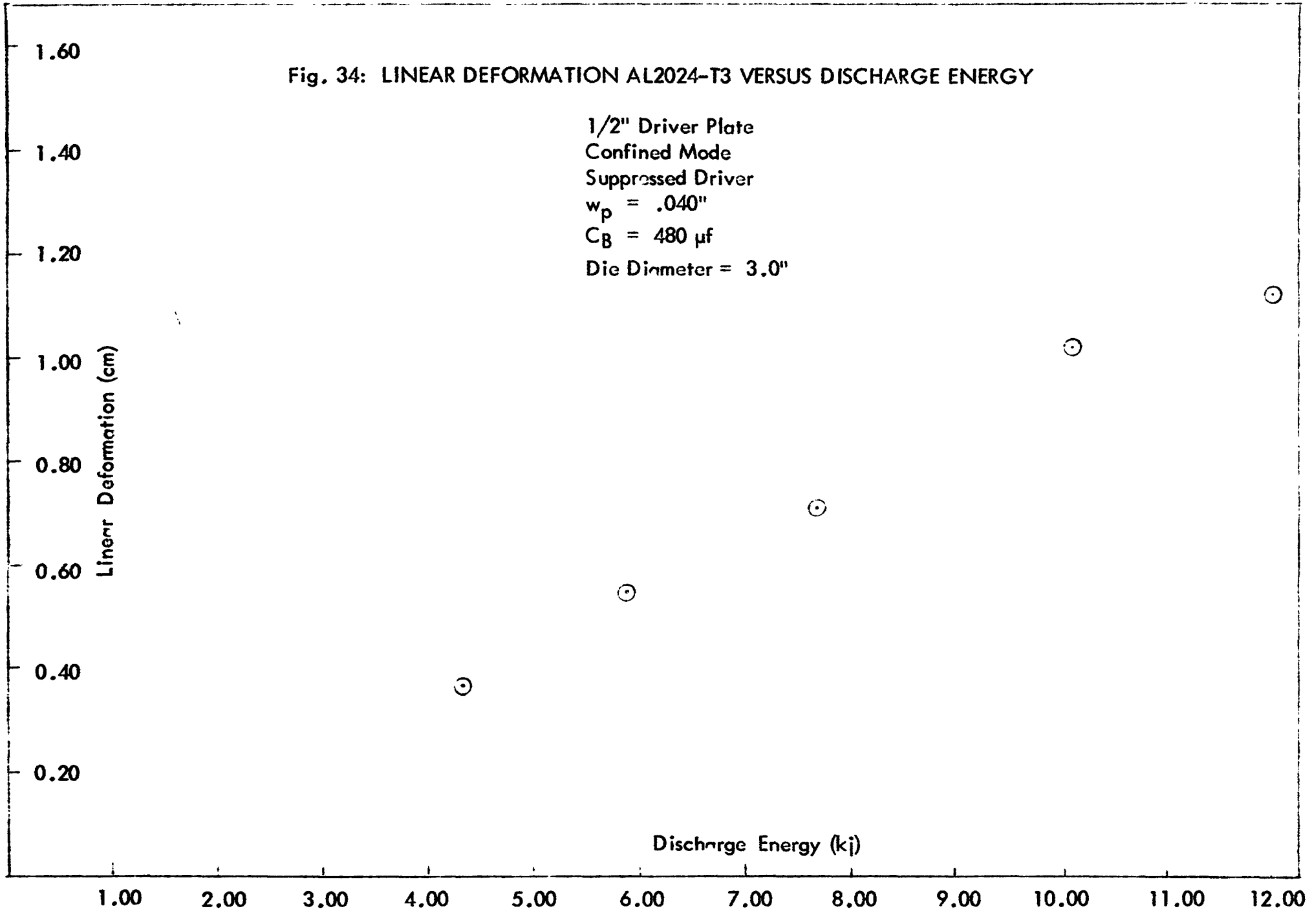

Fig. 35: LINEAR DEFORMATION AL2024-T3 VERSUS DISCHARGE ENERGY

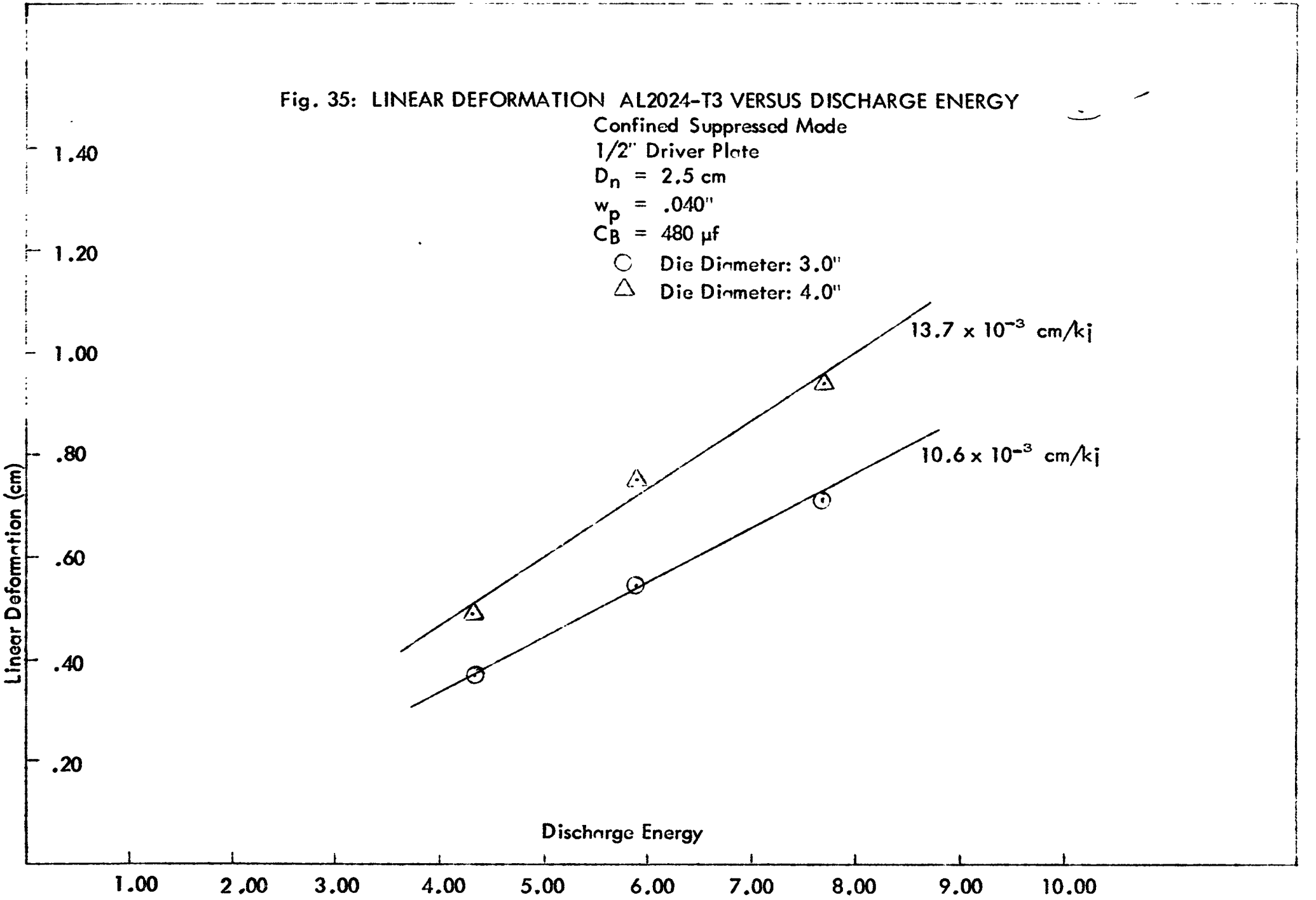

Fig. 36(a): The SS15-1 Section of the Current Multiplier Switch

Fig. 36(b): The "Maker Switch" on Closing Section of the Current Multiplier. When closed the load is in parallel with all sections of the coil.

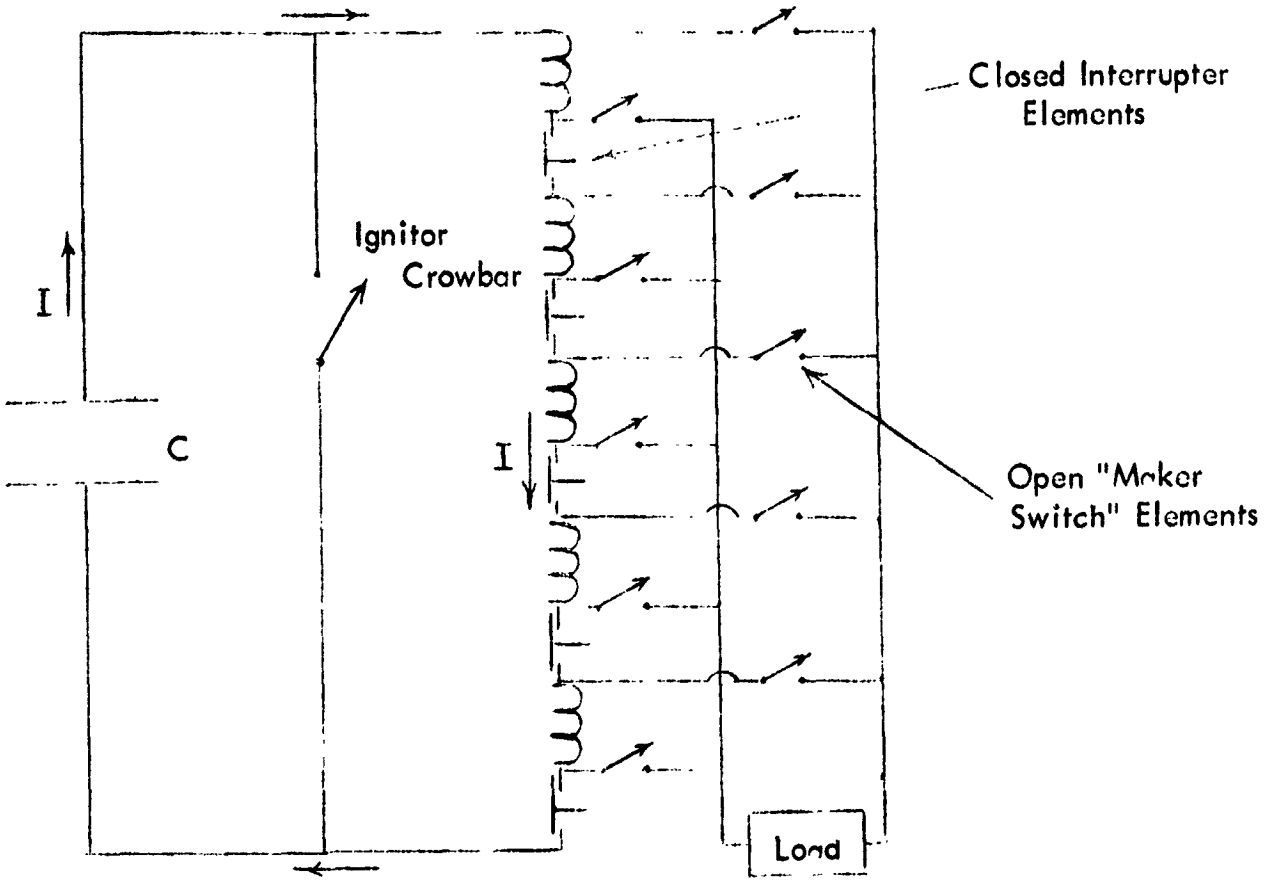

Fig. 37(~): CHARGING CIRCUIT

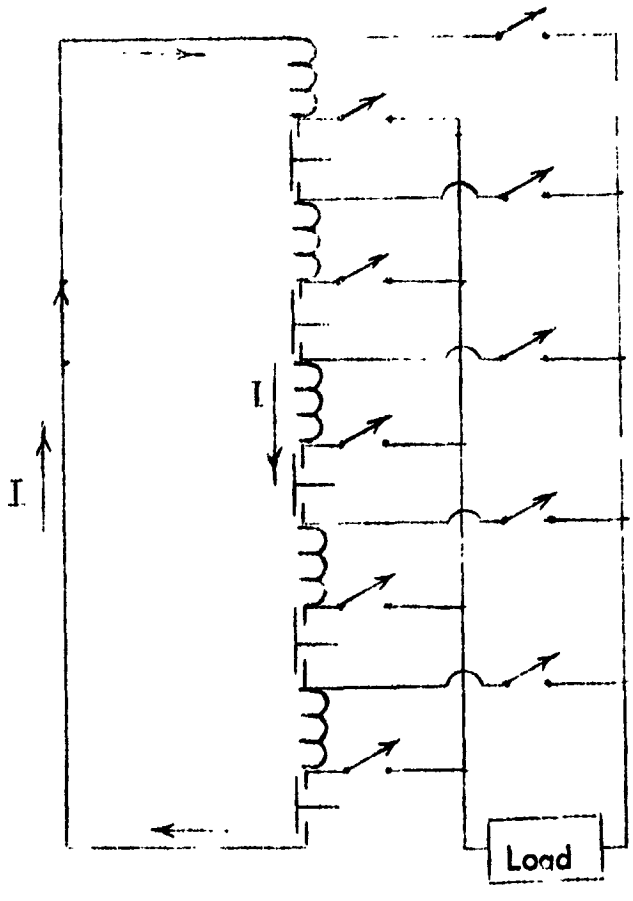

Fig. 37(b): CROWBAR CIRCUIT

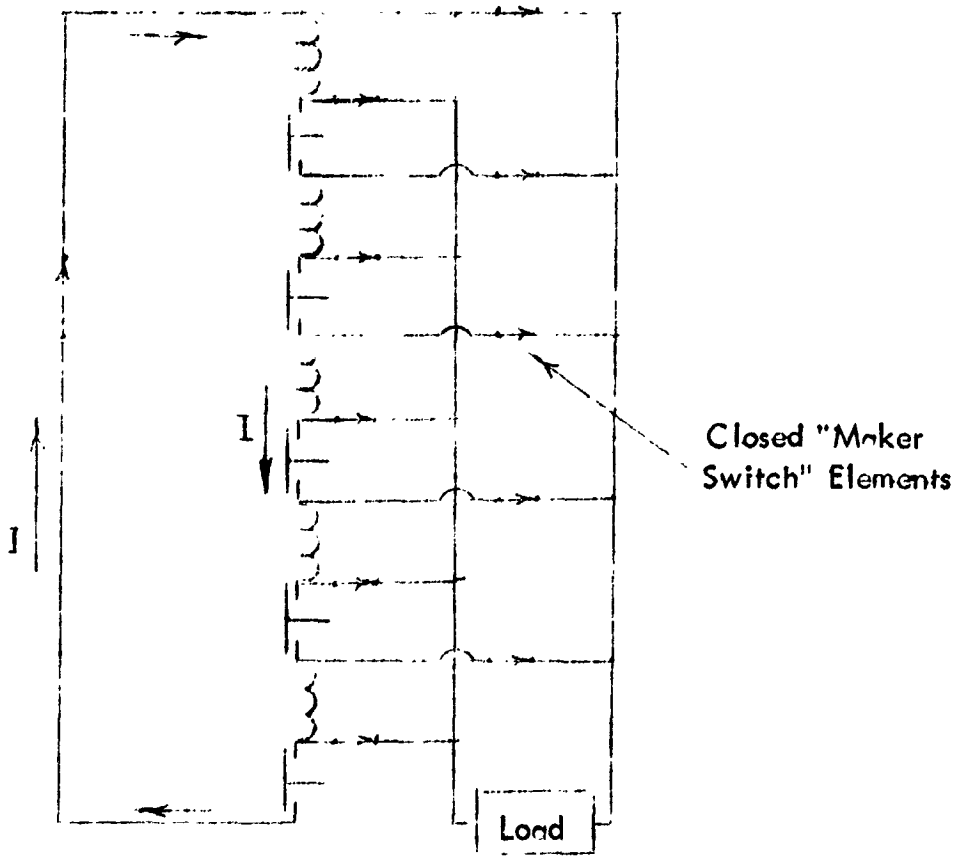

Fig. 37(c): INTERMEDIATE SWITCHING CIRCUIT

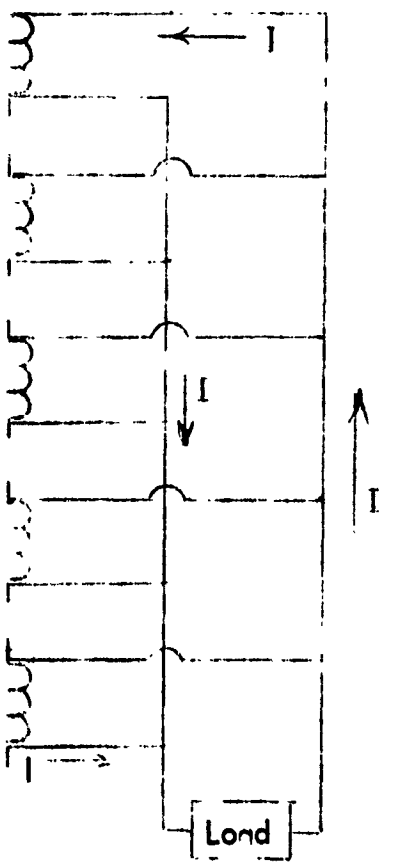

Fig. 37(d): DISCHARGE CIRCUIT

Fig. 38: Voltage Pickup Without Switching

Upper: Voltage across resistor in charging and crowbar circuit.
1 v/cm
10 msec/cm

Lower: Voltage across equal resistance in discharge circuit.
1 v/cm
10 msec/cm

Fig. 39: Voltage Pickup With Switching

Upper: Voltage across resistor in charging and crowbar circuit.
1 v/cm
10 msec/cm

Lower: Voltage across equal resistance in discharge circuit.
1 v/cm
10 msec/cm